공학박사 학위논문

High performance nanocarbon field emitter

고성능 나노탄소 전계 방출 소자

2018 년 2 월

서울대학교 대학원

기계항공공학부

이 정 석

Abstract

High performance nanocarbon field emitter

Jeong Seok Lee

School of Mechanical and Aerospace Engineering

Seoul National University

By taking advantage of the superior material properties and high aspect ratio geometry of nanocarbon materials, many researchers have been able to devote their efforts toward the development of nanocarbon emitters, which are capable of providing low turn-on voltage, high emission current density and long-term emission stability. Electron beams of field emitter are widely employed in various applications, including X-ray photography and computed tomography (CT) scans in hospitals, fault detection of semiconductor devices, airport security, and terahertz generation. Moreover, electron beam generators are progressively becoming more miniaturized, light-weighted, and low-powered so that they can be applied to diverse areas. For a high performance field emitter, new concept of field emitter is needed to overcome the previous research. In this thesis, four novel approaches are developed in terms of fabricating the multidimensional field emitters.

1) CNT point emitter with graphene interfacial layer: we report graphene as an interfacial layer between the metal and CNTs to improve the interfacial contact. The interfacial graphene layer results in a dramatic decrease of the electrical contact resistance by an order of 2 and an increase of the interfacial thermal conductivity by 16%. Such a high improvement in the electrical and thermal interface leads to superior field emission performance with a very low turn-on field of 1.49 V μm^{-1} at 10 $\mu A\ cm^{-2}$ and a threshold field of 2.00 V μm^{-1} at 10 mA cm^{-2}, as well as the maximum current of 16 mA (current density of 2300 A cm^{-2}).

2) CNT line emitter using clamping process: we report a robust and scalable method to fabricate high-performance carbon nanotube (CNT) line emitters by using a macroscopic mechanical clamping process. The process utilizes a handheld, metallic tongs (which also serves as an electrode for field emission) to pick up vertically aligned, super-grown CNTs from a substrate. By applying mechanical compression to a CNT forest in the uniaxial direction, the hemicylindrical shape of CNT structure strongly held with the tongs electrode is fabricated. With robust mechanical, thermal, and electrical contact characteristics created by mechanical clamping of CNTs, the CNT line emitter shows superior field emission performance with an emission current of 43 mA, a current density of 2700 $mAcm^{-2}$, and stable operation over 10 hours. Furthermore, an extremely high emission current of 103 mA

is achieved by clamping multiple CNT forests in a single tongs, showing prompt applicability of the present emitter for high-power electron beam sources.

3) Holey graphene film as a planar field emitter: we introduce an emitter in the shape of a hole, or hole emitter. An array of holes in graphene film can serve as a planar emitter, in which each circular hole is an emitter. Because of the nature of the sidewall emission through the edge of graphene film, the present planar emitter does not need any cumbersome process of leveling off emitter height and contriving to obtain the desirable inter-distance between emitters. Therefore, the screening effect and the field emission uniformity considered as obstacles in developing high efficiency planar emitters are easily resolved by an optimal design of the circular hole array. Moreover, the graphene film emitter is so flexible that it can be wrapped around a cylindrically shaped anode. This flexibility allows the present emitter to be used as a high power electron beam source because of the focusing of the emitted electron beams rendered by the concavely curved surface.

4) Carbonized cork emitter for multi-dimensional field emission: to broaden the range of application of electron beams, low power field emitters are needed that are miniature and light. We introduce here carbonized cork as a material for field emitters. The light natural cork becomes graphitic honeycomb upon carbonization, with the honeycomb cell walls 100-200 nm

thick and the aspect ratio larger than 100, providing an ideal structure for the field electron emission. Compared to nanocarbon field emitters, the cork emitter produces a high current density and long-term stability with a low turn-on field. The nature of cork material makes it quite simple to fabricate the emitter. Furthermore, any desired shape of emitter tailored for the final application can easily be prepared for point, line, or planar emission.

Keywords: field emission, point emitter, line emitter, planar emitter, interfacial layer, graphene, CNT, turn-on field, current density

Student Number: 2009-20709

Contents

List of Figures

Chapter 1. Introduction

Electron beams are widely employed in various applications, including X-ray photography and computed tomography (CT) scans in hospitals, fault detection of semiconductor devices, airport security, and terahertz generation.[1-3] Moreover, electron beam generators are progressively becoming more miniaturized, light-weighted, and low-powered so that they can be applied to diverse areas.

In most general sense, electron emission results from directing energy in the form of light, heat, high electric field, of collisions to a material in such a way that electrons within he material are given enough energy to overcome an energy barrier or work function. There are generally two type of the electron emission depending on the methods of energy transfer to the electrons. One is thermionic emission, which can emit electron from the surface, resulting from the surface are heated to high temperature about 1,000 ℃. The other is called the field emission. The strong local electric field applied on the surface extract the electrons even at the zero temperature.

Although thermionic emission, an emission resulting from heating a source to a high temperature, is the most common way of generating an electron beam, it is yet to overcome disadvantages such as high power consumption, complicated structure, and difficulty in operation.[4, 5] Unlike the thermionic

emitter, it is not necessary to heat the tip, which presents many advantages over thermionic emission. As field emitters do not require heating to generate electrons, they are more energy efficiency. The cold nature of the emission prevents thermal drift of the cathode, allowing better and more stable electron focusing. Recently, most attempts to use field emission in high performance field emitter (high current density, high total current, low turn-on field) have been unsuccessful because of the screening effect and insufficient height leveling due to the random structure.

Carbon-based nano-materials have been utilized to relieve these limitations. With excellent mechanical, electrical, and thermal properties of these carbon-based materials, and their natural sharp edges that are highly suitable for focusing electric fields, excellent field-emission performance should result such as low turn-on electric field, high emission current density, and long-term stability.[6-8] In particular, CNT and graphene, a sheet consisting of sp^2-hybridized carbon atoms, is receiving much attention due to its superior electric field enhancement capability, originating from the atomically sharp edges of its structure.[9, 10]

Various methods have been developed to form a structure that is suitable for field emission such as direct growth, electrophoretic deposition (EPD), ion-mediated assembly (IMA), spin coating, screen printing, and transfer processes.[11-24] These methods, however, require a high-temperature chemical

vapor deposition (CVD) process, a complicated oxidation process to make the solution, or a cumbersome transfer process which makes fabrication very difficult. The nanocarbon sheets in the structure fabricated by these methods are usually randomly oriented and the protruding sheets cause a local concentration of electric field, leading to excessive field emissions and eventually destruction due to Joule heating.[25, 26] Presence of randomly oriented dense sheets, on the other hand, decreases the electric field due to screening effect,[27-29] resulting in an inefficient electric field distribution and hence imposing a limit on the field emission enhancement.

In this thesis, we have evaluated the figure of merit of field emitter in terms of current density and turn-on field. (Figure of merit $= \frac{current\ density}{turn-on\ field}$) In addition, we have conducted to enhance the total current of field emitter for commercial applications. To accomplish the intended goal, four novel approaches are developed in terms of fabricating the field emitters of high figure of merit and total current. With the features of high figure or merit and total current comparable to commercial devices, the nanocarbon field emitter introduced here would broaden the range of electron beam applications and bring the emitter closer to our daily lives.

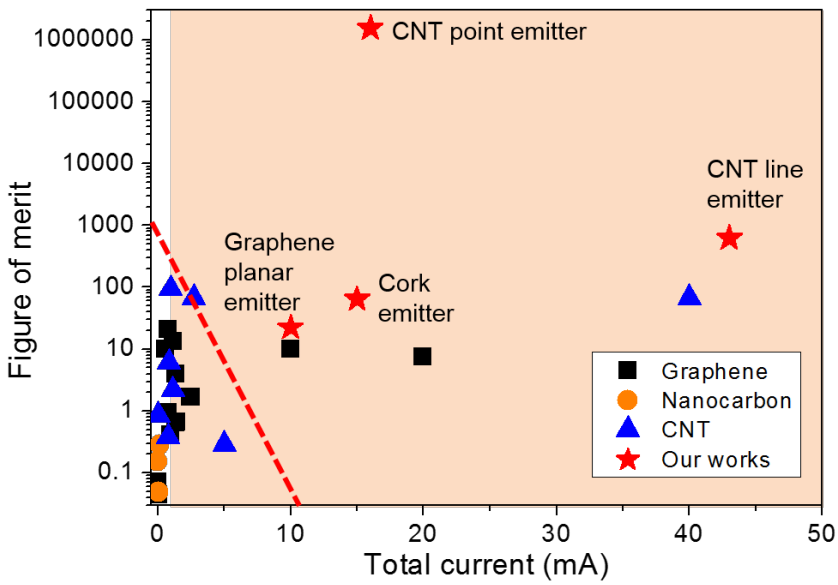

Figure 1-1. The figure of merit of nanocarbon field emitter as a function of the total current.[11-24, 139-149]

Chapter 2. CNT point emitter with graphene interfacial layer

Carbon nanotubes (CNTs) have great potential in the development of high-power electron beam sources. However, for such high-performance electronic device, the electric and thermal contact problem between metal and CNTs must be improved. To achieve high figure of merit and high current, we have investigated the point type 1-D structure for high field enhancement factor and the interfacial layer for better contact. Here, we report graphene as an interfacial layer between metal and CNTs to improve the interfacial contact. The interfacial graphene layer results in dramatic decrease of electrical contact resistance by an order of 2, and the increase of the interfacial thermal conductivity by 16%. Such a high improvement in electrical and thermal interface leads to the superior field emission performance with a very low turn-on field of 1.49 V/μm at 10 $\mu A/cm^2$ and a threshold field of 2.00 V/μm at 10 mA/cm^2, as well as the maximum current of 16 mA (current density of 2,300 A/cm^2).

2.1 Background of CNT point emitter

By taking advantages of the superior material properties and high aspect ratio geometry of CNT (carbon nanotube) [30], a great deal of research has been devoted to the development of CNT point emitters which are capable of providing low turn-on voltage, high emission current density and long-term emission stability [31-35]. Extremely high current density of the point emitter plays an essential role of a sufficient power source in microwave amplifier tubes, high-resolution electron-beam instruments and X-ray sources [36].

A CNT point emitter generally has a configuration of one-dimensional CNT structure at a conductive metal tip. The adhesion method of CNTs at a metal tip is appropriate for the fabrication of the point emitter when considering the quality issues of CNTs in the growth method [37, 38]. The CNT point emitters based on the adhesion method were fabricated either by the wet-spinning of CNT fibers [39], the crystal-like growth method [40], or attaching CNTs using dielectrophoresis [41] utilizing well-dispersed CNT colloidal solutions. However, the method usually results in emitters with high thermal and electrical contact resistances between metal and CNT, which seriously degrade field emission performances of the emitters [42-44]. High electrical contact resistance not only increases electric field for electron emission but also causes electrical Joule-heating at the contact interface. High thermal

contact resistance frequently decreases life time of the emitter due to sublimation of CNTs [20, 45].

Various efforts have been devoted to improve the electric and thermal interfaces between metal and CNTs. The efforts include metal welding to CNTs using ultrasonic bonder [46], an additional carbon layer deposition using EBID (electron beam-induced deposition) [47] and depositing graphitic layer via heat treatment at the temperature above 880 K [48]. Though various methods [49, 50], in addition to those mentioned above, could reduce the electrical contact resistance by an order of 1 to 3; however no attempt was made at reducing thermal resistance. In addition, they usually require high temperature process or additional cumbersome treatments. A simple and effective method to improve the interface between metal and CNTs is necessary.

In the present study we have investigated graphene as an interfacial layer between metal and CNT to improve the interfacial contact properties. Single layer graphene has remarkable electron mobility (~150,000 $cm^2/V•s$) and thermal conductivity (~3,100 – 5,300 W/m•K) [51, 52]. Moreover, since graphene is a two dimensional material and basically consists of the same atomic structure as CNT, exhibiting a similar work function of ~4.5 eV [53, 54], graphene has a great potential for the interfacial layer to improve the electric and thermal interfaces between metal surface and CNTs. Adopting graphene to interfacial layer between metals and CNTs, we successfully achieved a

dramatic decrease of electrical contact resistance by an order of 2, and the increase of the thermal conductivity by 16%. The performance of CNT point emitter including the graphene interfacial layer is also greatly improved.

2.2 Experimental section

SWNTs (ASP-100F, Hanwha Nanotech Corp.) were sonicated in HNO_3 (nitric acid) for 1 hour. The wet acid treated SWNTs were mixed with deionized water for neutralization. Then the mixture filtered on a membrane filter (Millipore, 0.2 μm pore size, 47 mm diameter) with a vacuum filtration method. The SWNTs which dried in a vacuum chamber at 80°C and sodium tungstate ($Na_2WO_4 \cdot 2H_2O$, Sigma Aldrich) dissolved in an organic solvent of N,Ndimethylformamide (DMF) with 0.1 mg/ml on sonicator for 10 hour. Meanwhile, a 300 μm copper wire (The Nilaco Corporation, Japan) was electrochemically etched in KOH solution (1.5 M) with an applied voltage of 20 V to produce a sharpened copper tip.

Graphene monolayer was grown on 300 μm copper (Cu) wires using low-pressure chemical vapor deposition. Briefly, copper wire was annealed at 1000°C at 0.1 Torr with a H_2 flow of 6 sccm for 30 min, and then CH_4 (105 sccm) introduced for 20min. After growth, copper wires were cool down to room temperature while the gas was maintained.

The copper tip is submerged in n,n-DMF solution consisting of CNT and sodium tungstate, and then electric current of 1 mA is applied. Due to the applied bias between the copper tip and counter electrode, negatively charged CNTs gather around the copper tip with WO_4^{2-}. After the submergence of 5 minutes, the copper tip is extracted and a droplet including CNT and WO_3 composite is formed at the end of the copper tip. The droplet is in the form of a gel and moved to have a contact with the teflon surface, resulting in vertically aligned one-dimensional composite structure after drying process.

The field emission characteristics were measured at room temperature under 3×10^{-7} Torr. A voltage between the CNT cathode and an anode was applied using DC power supply (Matsusade Precision INC.). The plate-shape molybdenum (Mo) was used as the anode. The emission current was measured by using a multimeter (KEITHLEY 2000). The distance between cathode and anode was fixed at 500 μm by separator. SEM analysis was performed using a Hitachi S-4800 field-emission electron microscope at an acceleration voltage of 10-15 KeV. Raman spectra were obtained using a micro Raman system (JY-Horiba, LabRam 300) with a 50X objective lens (Olympus, NA 0.75).

2.3 Result and discussion

A CNT point emitter was fabricated by the crystal-like growth method [40, 55] using a copper wire tip as shown in Figure 2-1. The tip of the copper wire was sharpened by electro-chemical etching [56] (Figure 2-1(a)) followed by a graphene synthesis on the wire using CVD process with H_2 and CH_4 gas flows at 1000°C (Figure 2-1(b)) [57]. Figure 2-1(c) shows the experimental procedure to fabricate the CNT point emitter based on single-walled CNT (SWNT) colloidal solution mixed with sodium tungstate[40]. The SWNTs have a length of 5-10 μm and the average bundle diameter of SWNTs is determined from transmission electron microscopy (TEM) analysis as being 7 nm (Figure 2-2). Upon applying bias between copper tip and counter electrode, CNTs negatively charged through purification process and WO_4^{2-} migrate to the copper tip. WO_4^{2-} changes into WO_3 during the plating process, encouraging tight contact between adjacent CNTs as well as CNT and graphene surface. An electron probe microanalysis (EPMA) technique reveals that the tungsten and carbon are uniformly distributed all over the composite structure in which the WO_3 was electroplated on the SWNT wall [40]. After electroplating process, the copper tip is withdrawn with a droplet including CNT and WO_3 composite. The droplet is placed on a Teflon surface to constrain the free end of droplet,

resulting in a straight one-dimensional composite structure after solvent evaporation.

The composite structure is finally detached from the Teflon surface as shown in Figure 2-1(d), then the resulting emitter has a cylindrical geometry with a diameter of ~30 μm, of which the length can be controlled by adjusting the plating time [40]. The “nail head” geometry (see the tip of the CNT emitter in Figure 2-1(d)) is formed due to the contact-drying process that is necessary to make the structure straight. The “nail head” can be removed by a post-processing treatment. As shown in the inset of Figure 2-1(d), the CNTs are well aligned along the emitter axis. CNTs, which are randomly dispersed in the solution, are aligned in the direction of the emitter during the crystal-like growth process [40]. Since the alignment is made in the direction of electron path during the field emission, the self-alignment helps to enhance performances of the emitter.

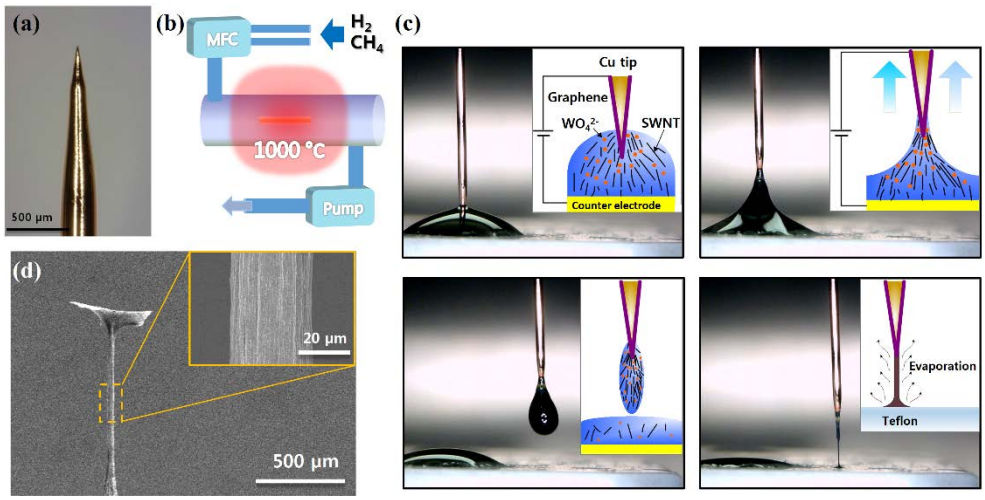

Figure 2-1. (a) An optical image of sharpened copper wire using electro-chemical etching process. (b) Schematic drawing to fabricate the graphene growth by chemical vapor deposition (CVD). (c) Optical images of carbon nanotube point emitter through crystal-like growth method. (Inset shows Schematic drawing of crystal-like growth method) (d) SEM image of the point emitter that is comprised of aligned carbon nanotube with one direction.

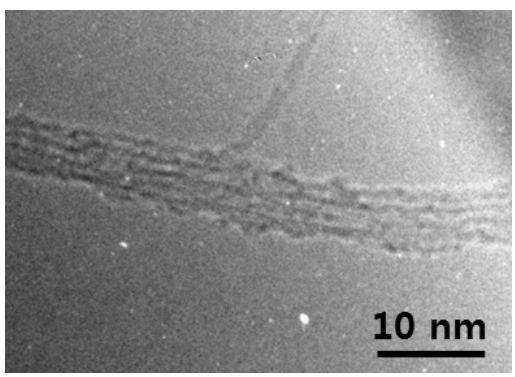

Figure 2-2. Transmission electron microscopy (TEM) image of the SWNT bundle.

It is the most important step in the present study that the high quality graphene is uniformly synthesized on the surface of the copper wire before the crystal-like growth of the CNT emitter. The inset of Figure 2-3(a) shows the optical image of the copper wire after the synthesis of graphene layer. To confirm a graphene layer on the copper wire, Raman analysis was carried out as shown in Figure 2-3(a). The Raman peaks characteristic of G-band (~1579 cm^{-1}) and 2D-band (~2693 cm^{-1}) of graphene are clearly observed over a broad background signal of copper. Almost identical Raman characteristics were observed along the length direction of Cu wire including the cone-shaped region, confirming the uniform growth of graphene on the wire (Figure 2-4). The graphene was transferred onto a silicon substrate to exclusively analyze the characteristics. The inset of Figure 2-3(b) shows the optical image of the graphene transferred to a silicon substrate after etching the copper wire and drying it at ambient condition. The cylindrical structure of the graphene wrapping around the copper wire was collapsed into a ribbon geometry during the transfer process. The Raman spectra of the transferred graphene are shown in Figure 2-3(b). The intensity of the D band at ~1350 cm^{-1} is negligible and the 2D/G ratio was estimated to be ~2.1, indicating that 1 or 2 layers of high quality graphene was successfully synthesized on the copper wire [58]. Atomic force microscopy (AFM) study also revealed a thickness of ~1 nm for the graphene layer, as determined by the Raman analysis (Figure 2-5).

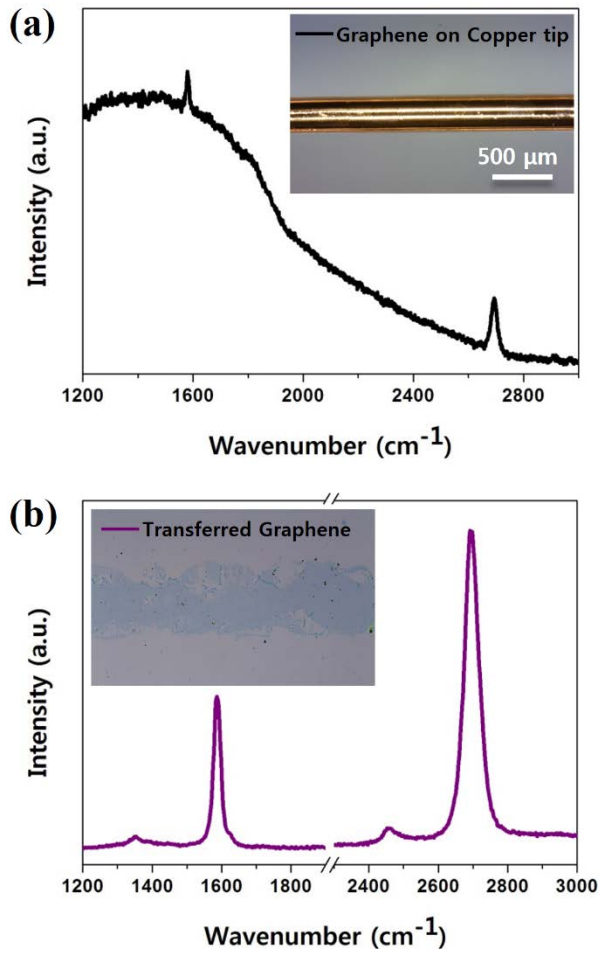

Figure 2-3. (a) Raman spectrum of graphene on copper tip obtained by 532-nm photo-excitation. (Inset shows an optical image of copper wire after graphene growth.) (b) Raman spectrum of transferred graphene on silicon substrate obtained by 532-nm photo-excitation. (Inset shows an optical image of transferred graphene to silicon substrate.)

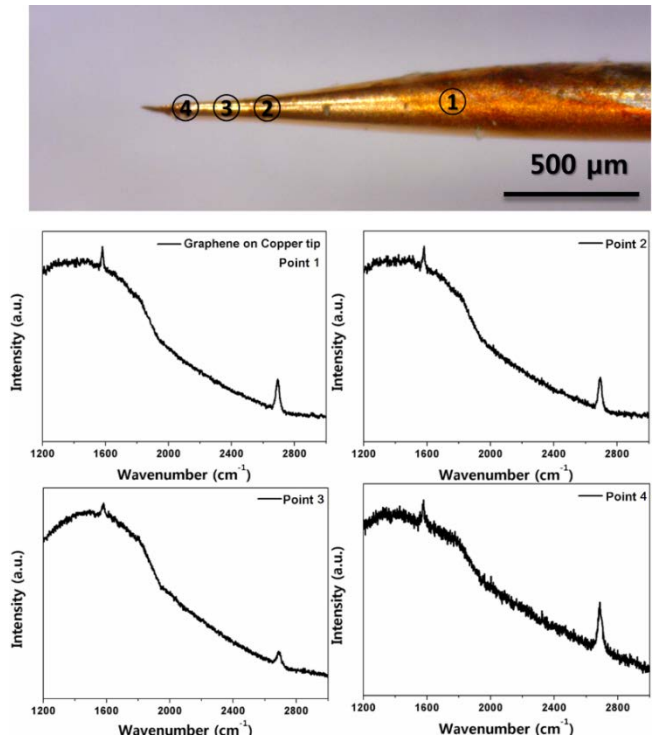

Figure 2-4. Raman spectra along the length direction of Cu wire.

.

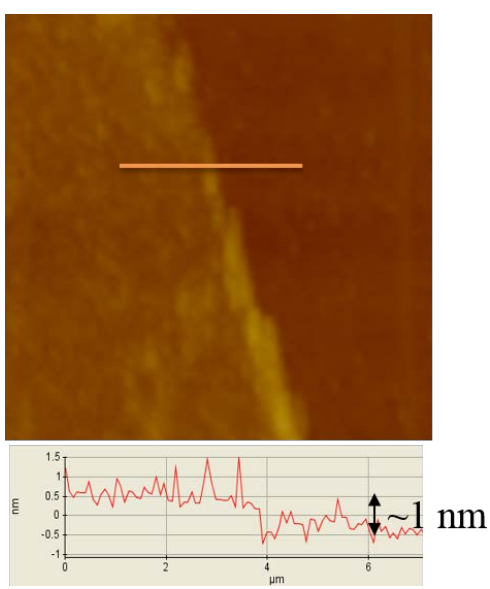

Figure 2-5. AFM image of the transferred graphene onto SiO_2 substrate.

The effectiveness of graphene interfacial layer for electrical and thermal contacts was demonstrated as shown in Figure 2-6. The total electrical resistance of the CNT point emitter consists of the resistances of copper wire, CNT structure and the interfacial contact resistance between the copper tip and CNTs, as schematically described in the inset of Figure 2-6(a). The contact resistance was evaluated by subtracting resistances of the copper wire and the CNT structure from the total resistance of the emitter. The contact resistance of the emitter without graphene was 2.39 kΩ, which corresponds to most of the total resistance (2.40 kΩ), while the emitter with the graphene interfacial layer shows 25 Ω of the total resistance, having a very low contact resistance of 14 Ω. It is noteworthy that the contact resistance of the emitter with the graphene interfacial layer is 2 orders of magnitude lower than that without the layer.

Since the field emission stability of a CNT emitter is degraded by sublimation of CNTs at the end of the emitter, high thermal conductivity of the emitter is very important so that it rapidly dissipates heat generated during emission. The thermal interfacial resistance of the present emitter was investigated by comparing the thermal conductivity of the emitter with and without graphene interfacial layer as shown in Figure 2-6(b). The emitters with and without graphene interfacial layer prepared with the same geometry (i.e., the emitter length and diameter), were placed in a vacuum chamber (~ 10^{-3} torr) to

minimize heat convection effect of air. The controlled temperature was applied to the end of the copper wire using electrical Joule-heating of chromium wire (see the inset of Figure 2-6(b)). The temperatures of copper wire (T_1) and the CNT emitter tip (T_2) were measured using a thermocouple by making a contact with thermally conductive epoxy. Figure 2-6(b) shows the temperature differences ($\Delta T = T_1 - T_2$) with respect to the applied temperature to the copper wire. The thermal conductivity ratio can be expressed as the inverse of the temperature change ratio ($K_w/K_{w/o} = \Delta T_{w/o}/\Delta T_w$) based on heat conduction equation, where K represents thermal conductivity and the subscripts w and w/o denote with and without graphene interfacial layer, respectively. The temperature change shows linear relationship with respect to the applied temperature. It is noteworthy that the use of graphene interfacial layer increases thermal conductivity of the emitter by 16% as shown in Figure 2-6(b).

In metals with poor wettability such as Pt, Ni, Ag, and Cu, the contact barrier (such as vacuum gap, surface oxides) is easily formed between metal and CNT [59]. Van der Waals force is not large enough to make complete physical contact between copper and CNT, as previously observed in dewetting phenomena of CNT and metal contacts [60, 61], where an atomic-level vacuum gap was observed. The atomic-level vacuum gap results in large electrical contact resistance [62]. However, if we prepare copper with the surface covered

by synthesized graphene layer through carbon segregation and/or precipitation process, the graphene automatically has maximized contact area with copper. Moreover, the graphene has not only ohmic contact with CNT because of almost identical work function but also large contact area with CNT due to the van der Waals forces and π-π stacking interactions [63, 64]. As a consequence, the adoption of graphene interfacial layer results in very low contact resistance of the emitter.

To confirm the effect of contact area between copper and CNTs, we prepared three specimens with different stacking sequences: 1) copper and CNT, 2) copper, transferred graphene and CNT, 3) copper with synthesized graphene and CNT, and measured their electrical contact resistance as shown in Figure 2-6(c-d). The CNT layer is simply stacked by placing a thin CNT film on the specimens. The contact resistance between copper and CNT with synthesized graphene interfacial layer is 150 times lower than that without the graphene layer, and 10 times lower than that with transferred graphene interfacial layer. The lower contact resistance with graphene layer than without graphene layer could be attributed to the increased contact area and π-π stacking interactions due to graphene interfacial layer. Moreover, it is clear that the synthesized graphene interfacial layer allows larger contact area between copper and graphene than the transferred graphene layer. It is believed that metal-based contamination or wrinkles occurred during the wet transfer process adopted

in this test causes physical gap between the copper and the transferred graphene layer [65, 66].

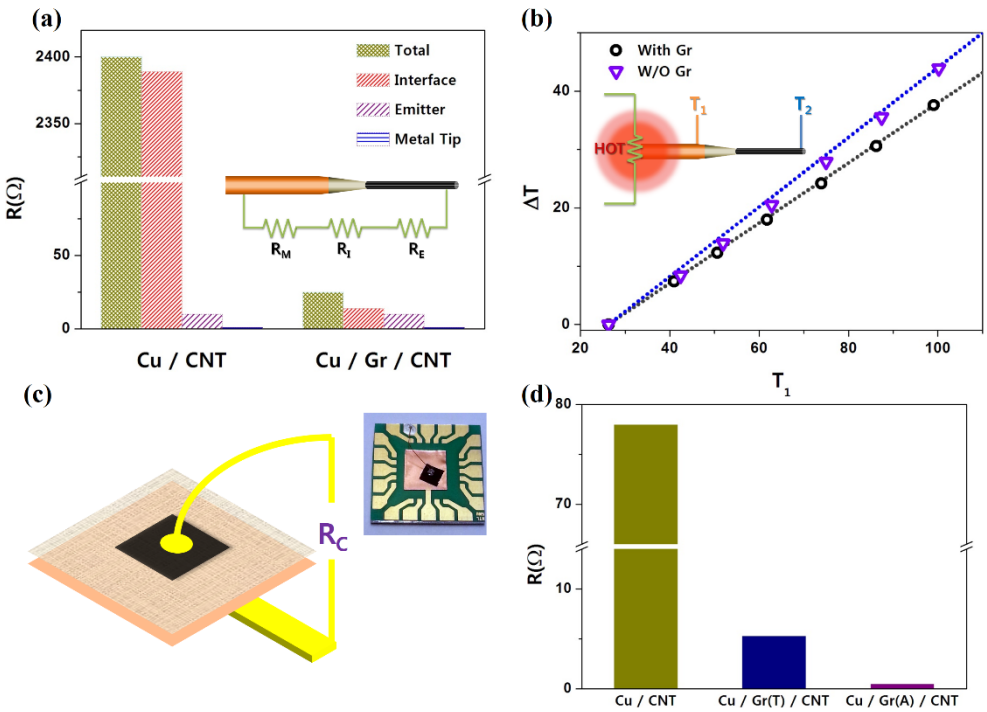

Figure 2-6. (a) Graph shows the change of resistance due to the graphene interfacial layer. (Inset shows three electrical resistance components: R_M is resistance of copper wire, R_I is interface resistance and R_E is resistance of point Emitter. (b) Graph shows the improvement of heat conductivity by 16 % with the graphene interfacial layer. (Inset shows schematic drawings of thermal conductivity measurement.) (c) Schematic drawing and optical image to measure the electrical contact resistance. (d) Comparison of contact resistance between the copper and CNT with and without graphene layer (Gr(T) is transferred graphene layer, and Gr(A) is as-grown graphene layer.)

The improved interface with graphene layer may enhance the field emission performance of the present emitter. The effect of adopting graphene layer to the emitter was investigated with respect to field emission performance. The nail head geometry of the emitter tip shown in Figure 2-1(d) results from a pinning effect and capillary flow in which contact line of the drying column on the Teflon surface is replenished by solvent from the interior as the solvent evaporates from the edge. The nail head geometry at the tip of the emitter is not desirable for a point emitter because it degrades electric field concentration and structural robustness. EDM (electric discharge machining) process could be utilized to remove the nail head [55]. However, a very high current (~7 ampere) that passed through the CNT emitter might degrade the electrical properties of CNT emitter. Thus, we adopted focused ion beam (FIB) treatment to remove the nail head. It was severed from the emitter by the irradiation of Ga ion beam with high energy. The emitter without the nail head is clearly shown in the SEM image of Figure 2-7(b) which has a diameter of 30 μm. From the SEM observation of Figure 2-7(c), the severed surface is formed in a very consistent and regular manner, textured in the direction of beam irradiation. Raman analysis was carried out to investigate the effect of FIB treatment on the surface of the CNT emitter tip. In the Raman spectra of the emitter before and after the FIB treatment, the change of G/D ratio is

insignificant. The slight increase of D peak could be attributed to physical damage on CNT due to Ga ion collisions.

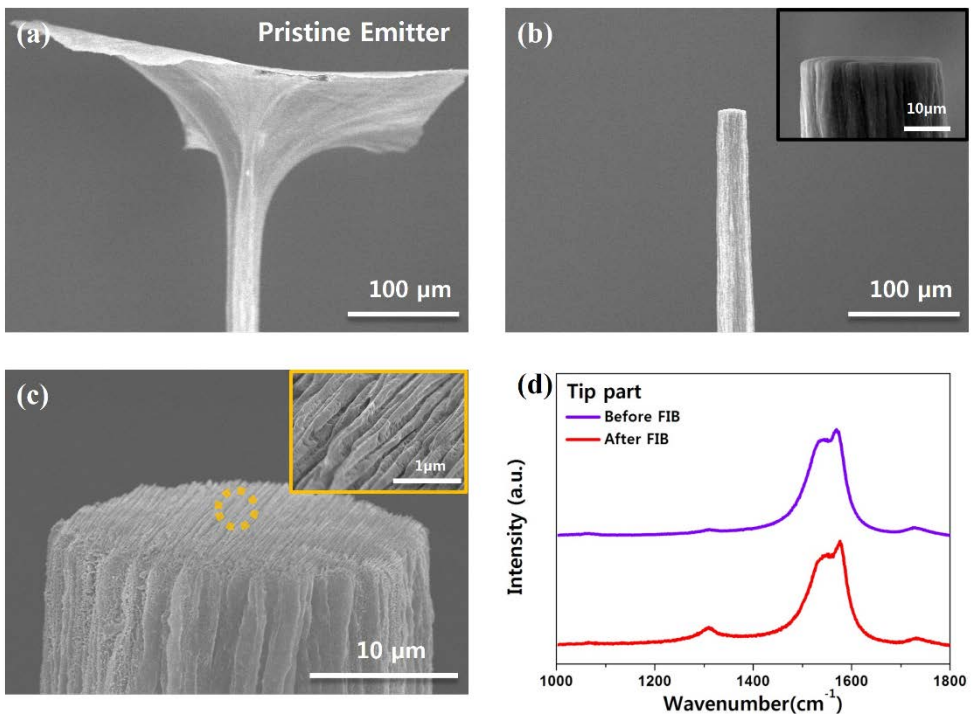

Figure 2-7. (a) Scanning electron micrograph of the pristine emitter with nail head. (b) Scanning electron micrograph of the emitter with the nail head removed by FIB treatment. (c) The close up scanning electron micrograph of the cross-section area with FIB treatment. Inset image shows the trace of Ga ion during FIB treatment. (d) Raman spectra obtained by 532-nm photo-excitation at the cross-section area of carbon nanotube point emitter of two cases, before FIB and after FIB treatment.

Figure 2-8 shows the field emission characteristics of the CNT point emitters. The distance between cathode tip and anode (d) was used to calculate the macroscopic field (E=V/d, where E and V represents an applied electric field and voltage) [33]. It is noteworthy as shown in Figure 2-8(a) that the turn-on field (E_{on}: 1.49 V/μm at 10 μA/cm^2) and the threshold field (E_{th}: 2.00 V/μm at 10 mA/cm^2) of the emitter with graphene interfacial layer are considerably lower than those without graphene interface (E_{on}: 2.74 V/μm, E_{th}: 3.25 V/μm). Moreover, the maximum current of the emitter with graphene interfacial layer reaches up to 16 mA which corresponds to the current density of 2,300 A/cm^2, while it is 6 mA for the emitter without graphene interface. It is obvious that the improved electrical and thermal contacts between the copper wire and the CNT emitter are responsible for the enhancement of the emission performance. Figure 2-8(b) shows Fowler-Nordheim (F-N) curves of the emission and the slope of F-N curve represents field enhancement factor of an emitter. The field enhancement factor of 2,120 for the emitter with graphene interfacial layer is almost two times higher than that of 1,180 for the emitter without graphene interface. The CNT emitter with high electrical and thermal conductivity is attributed to the excellent field emission characteristics. Moreover, it is interesting that two distinct behaviors regarding F-N curves were observed. The field enhancement factor of the emitters with and without graphene interface is almost linear in low field

region. However, it turns into nonlinear in the region of high electrical field because of thermally enhanced electron emission due to Joule-heating of the carbon nanotube [67]. Joule-heating at the tip of the emitter, which may exceed up to 1,000 K, adds thermionic emission current to the field emission, enhancing the overall emission performance [68].

The emission stability of the present emitter was investigated by continuously performing emission with a current of 1-5 mA for 10 hours, as shown in Figure 2-8(c) and (d). The current is not stable during the test in the emitter without graphene interface and considerable degradation was observed, for instance, 30% in 1 mA, 50% in 3 mA and 56% in 5 mA after 10 hours operation (Figure 2-8(c)). As shown in Figure 2-6(a) and (b), the emitter without graphene layer has high electrical and thermal resistance, especially at the interface. At a given field emission current for stability tests, the emitter without graphene layer demands higher electric field compared to that of the emitter with graphene layer, which in-turn leads to severe heat accumulation. It might lead to oxidize and/or severely degrade the emitters by Joule-heating [69]. However, the emission stability is significantly improved when the emitter with graphene interfacial layer was used as shown in Figure 2-8(d). The reasonably small degradation in the current was observed after 10 hours operation such as 15% in 1 mA, 23% in 3 mA and 30% in 5 mA.

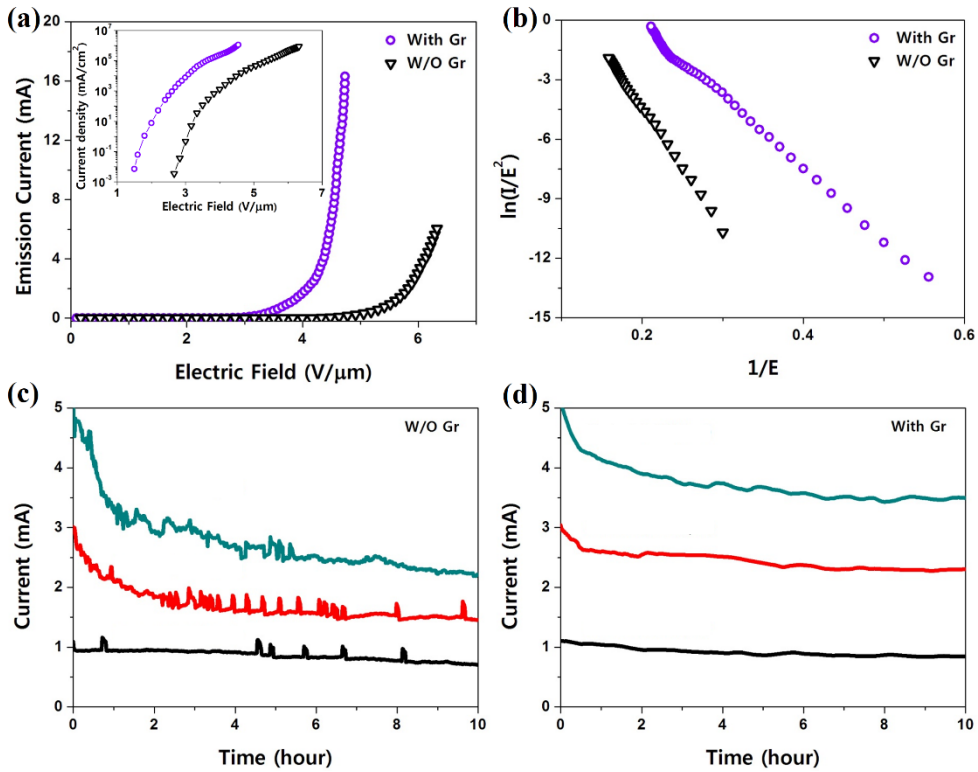

Figure 2-8. (a) I-V plots of point emitter with and without graphene interfacial layer. (Inset shows J-E plot with logarithmic current density) (b) Fowler-Nordheim plots of field emission characteristics (I-V plot). (c, d) Field emission stability test of the emitter without and with graphene interfacial layer.

2.4 Conclusion

The contact interface involved in fabricating a CNT point emitter is one of the important issues to be resolved. In the present study the adoption of graphene as an interfacial layer between metal and CNT has been investigated. High quality graphene was uniformly grown on a copper wire. The interfacial graphene layer results in dramatic decrease of electrical contact resistance by an order of 2, and the increase of the interfacial thermal conductivity by 16%. Such a high improvement in electrical and thermal interface leads to the superior field emission performance with a very low turn-on field of 1.49 V/μm at 10 μA/cm^2 and a threshold field of 2.00 V/μm at 10 mA/cm^2, as well as the maximum current of 16 mA (current density of 2,300 A/cm^2). The emitter also shows stable emission characteristics with a high current of 5 mA (700 A/cm^2) for 10 hours.

Chapter 3. CNT line emitter using clamping process

We report a robust and scalable method to fabricate high-performance carbon nanotube (CNT) line emitters by using a macroscopic mechanical clamping process. To achieve high figure of merit and total current, we have investigated the vertically aligned, super-grown CNTs for high current emission. The process utilizes a handheld, metallic tongs (which also serves as an electrode for field emission) to pick up vertically aligned, super-grown CNTs from a substrate. By applying mechanical compression to a CNT forest in the uniaxial direction, the hemicylindrical shape of CNT structure strongly held with the tongs electrode is fabricated. With robust mechanical, thermal, and electrical contact characteristics created by mechanical clamping of CNTs, the CNT line emitter shows superior field emission performance with an emission current of 43 mA, a current density of 2700 mA/cm^2, and stable operation over 10 hours. Furthermore, an extremely high emission current of 103 mA is achieved by clamping multiple CNT forests in a single tongs, showing prompt applicability of the present emitter for high-power electron beam sources.

3.1 Background of CNT line emitter

Many researches have clearly revealed that an individual carbon nanotube (CNT) is an excellent electron field emitter with a low turn-on field for emission, high emission current density, and long-term emission stability [70-74]. The superior emission characteristics stem from the unique one-dimensional structure and the extraordinary properties of CNT [30, 75-77]. Recently, various efforts have been made to enlarge the applicability of CNT emitters to industrial applications, including microwave amplifier tubes, high-resolution electron-beam instruments, X-ray, and terahertz power sources [36, 78, 79]. The structural geometry of the CNT emitter is also extended to non-planar prototypes by demonstrating wrappable CNT fiber, yarn, and sheet cathodes for field emission applications [80-82]. These recent advances in the CNT emitter have been synergistically accomplished with the development of macroscopic architectures based on assembled CNTs.

Various macroscopic forms of CNTs have been produced, including fibers, yarns, films, sheets and foams [80-85]. Each structure shows a unique geometry and functionality depending on the manner in which CNTs are assembled [86, 87]. The properties of individual CNTs are unrivaled by any other material; however, it has proven difficult to simultaneously retain the intrinsic property of CNT at engineering-relevant scales because of the assembly and the related

interface issues [88-90]. Moreover, several parameters need to be considered to design a high-performance CNT emitter, including not only the orientation, aspect ratio, uniformity, and density of CNTs, but also the physical contact of CNTs with a supporting electrode [31].

In the present study, a robust and scalable method is reported to fabricate high-performance CNT line emitters by using a macroscopic mechanical clamping process. The process utilizes a handheld metallic tongs to simply pick up vertically aligned, super-grown CNTs from a substrate. Upon mechanical compression to a CNT forest in a uniaxial direction, the clamped CNTs are compressed in the form of a densely packed CNT strip, while the CNTs anchored at a substrate are simultaneously detached from a substrate and are radially spread out similar to a bunch of flowers. As a result, the CNT structure is fabricated into a hemicylindrical shape, strongly held with the tongs electrode. The current mechanical clamping process allows the CNT emitter to consist of millimeter-scale, solely continuous CNTs and proceeds without inducing any defect on the CNTs. Therefore, the fabricated emitter is able to retain the intrinsic properties of CNT such as high electrical and thermal conductivity. With robust mechanical, thermal and electrical contacts created by the mechanical clamping process, the CNT line emitter shows superior field emission performances with an emission current of 43 mA, a current density of 2700 mA/cm^2, and a stable operation of over 10 hours.

Furthermore, an extremely high current of 103 mA is achieved by clamping multiple CNT forests in a single tongs, showing prompt applicability of the present emitter for high-power electron beam sources.

3.2 Experimental section

To prepare the growth substrate, an 18 nm thick aluminum (Al)-barrier layer was deposited on a (100) silicon (Si) wafer by electron beam (e-beam) evaporation. 1.0 nm thick iron (Fe) thin film as a catalyst for CNT growth is deposited by e-beam deposition over the Si substrate. The prepared growth substrate was inserted in the center of a 2 inch diameter quartz tube furnace. Vertically aligned MWNTs were synthesized at a growth temperature of 810˚C by introducing C_2H_2:Ar (210:480 sccm) gases for 16 min. Water vapor was introduced into the growth environment by passing a small fraction of the argon (Ar) carrier gas through a water bubbler. After the growth process, the furnace was cooled to room temperature while maintaining the gas flow.
A voltage between the CNT cathode and molybdenum (Mo) anode was applied using a DC power supply (Matsusada Precision Inc.). The field emission current was measured using a multimeter (KEITHLEY 2000). SEM analysis was performed using a Hitachi S-4800 field-emission electron microscope at an acceleration voltage of 10-15 KeV. Raman spectra were

obtained using a micro Raman system (JY-Horiba, LabRam 300) with a 50X objective lens (Olympus, NA 0.75).

3.3 Result and discussion

Figure 3-1 shows the procedure for the fabrication of a CNT line emitter. Vertically aligned, multi-walled carbon nanotube (MWNT) arrays were synthesized on a silicon substrate using water-assisted, chemical vapor deposition (CVD) with acetylene as the carbon source (see also Experimental section) [91]. The as-grown CNT forest has very low density (typically ~0.02 g/cm^3), whereby the CNTs only occupy 3.14% of the forest volume, enabling the CNT forest to be a highly compressible material. The MWNTs in the array have an average length of ~1.2 mm and the average diameter is determined as being 7 nm from transmission electron microscopy (TEM) analysis (Figure 3-2).

The clamping process for the CNT forest is schematically illustrated in Figure 3-1(a). A CNT forest specimen with a dimension of 0.4×0.4 cm^2 is placed in a metallic tongs that allows uniaxial compression in the lateral direction. The tongs made of stainless steel has high electrical (~1.0×10^6 Sm^{-1}) and thermal conductivity (~16 $Wm^{-1}K^{-1}$) so that it can be used directly as the electrode. A clamping depth of a CNT forest was easily controlled using a spacer. When

applying uniaxial mechanical compression to the upper part of the CNT forest, the individual CNTs in the forest are compressed and concurrently detach from the growth substrate. The lateral dimension of the CNT forest at the clamped region decreases uniaxially in the form of densely packed CNT strips (see the clamped part of CNT forest in Figure 3-1(c)). As the clamping force increases, the unclamped CNTs at the bottom part of the forest simultaneously undergo bending deformation in the vicinity of the clamp edges. Thus, CNTs reach radially outward from the line edge of the clamper as shown in the scanning electron microscope (SEM) images in Figure 3-1(b). As a result of this process, a hemicylindrical shape of CNT structure strongly held with the tongs electrode is achieved as shown in Figure 3-1(d).

The mechanical clamping method is highly productive and scalable, and is able to provide binder-free mechanical, thermal, and electrical contacts between the CNTs and the clamper. Moreover, the process allows a CNT structure consisting of solely continuous CNTs and proceeds without inducing structural damage to the CNTs. Raman analysis confirmed that the G/D ratios (~0.96) measured at the clamped CNT region before and after the clamping process were almost identical, as shown in Figure 3-3. This indicates that the CNT structure retains the intrinsic properties of the individual CNT, such as high electrical and thermal conductivity. Therefore, the present approach is advantageous for a variety of applications, especially

binder-free and high-performance CNT electrodes, and here we demonstrate their use as a CNT line emitter.

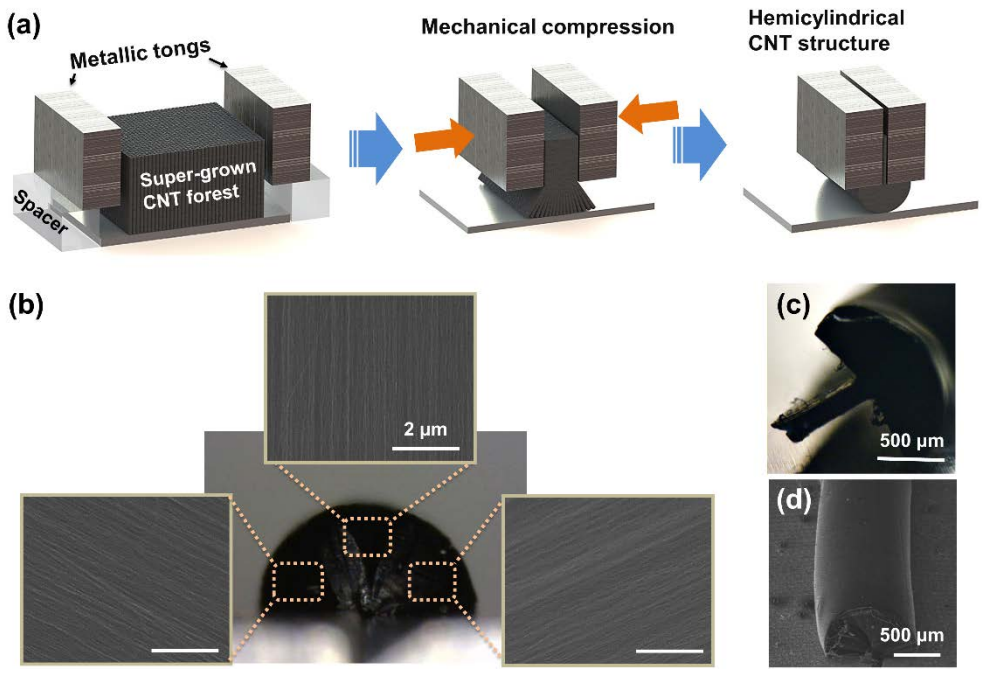

Figure 3-1. (a) Procedure illustrating for the fabrication of a CNT line emitter. (b) SEM images of CNTs reaching radially outward from a line edge of the clamper. (c) Optic image of the hemicylindrical CNT structure released from a tongs. (d) SEM image of the CNT structure clamped with a tongs.

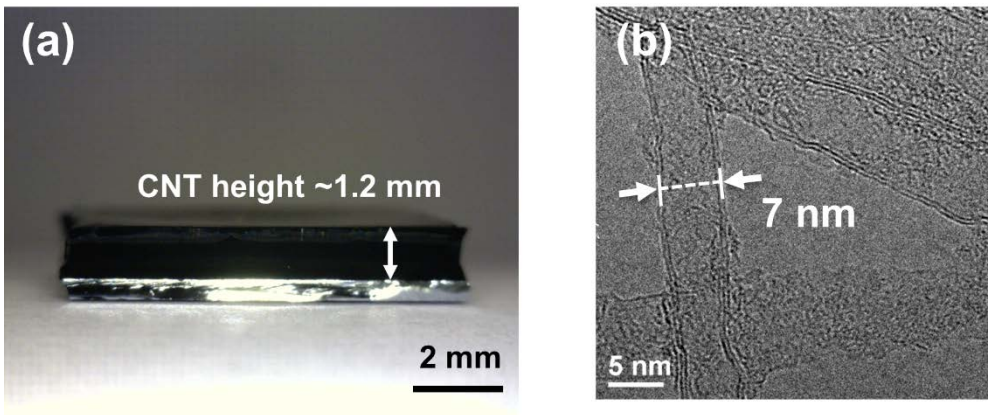

Figure 3-2. (a) Optic image of as grown CNT forest with a height of 1.2 mm, (b) TEM image of MWNTs showing a diameter of ~7 nm.

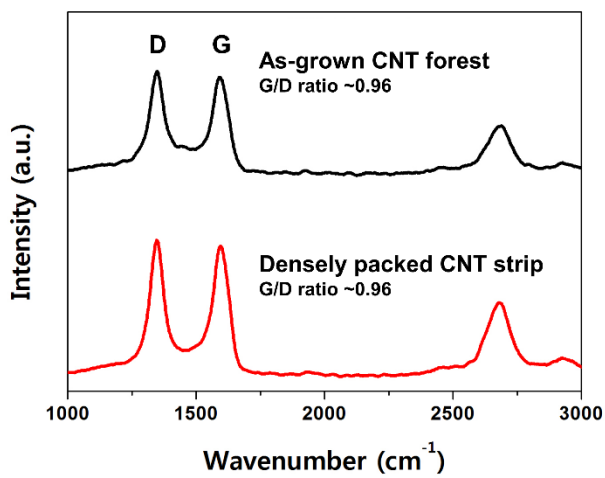

Figure 3-3. Raman spectra of the as-grown and clamped CNTs. Almost identical G/D ratios of ~0.96 are measured at the clamped CNT region before and after the clamping process.

It is worth noting that the density of CNTs on the circumference of the hemicylindrical structure depends on the radius of the structure. The radius of the CNT structure can be easily controlled by adjusting the clamping margin, which in turn is precisely controlled by the different spacer thicknesses (see Figure 3-4(a)). The field emission characteristics of CNT line emitters were measured in a vacuum chamber at a base pressure of 2.0×10^{-7} Torr. As the clamping margin increases from 300 to 700 μm, it was observed that the turn-on (electric field needed to produce a current density of 100 $\mu A/cm^2$) and threshold (current of 10 mA/cm^2) fields decreased from 6.9 and 9.2 V/μm to 5.4 and 7.7 V/μm, respectively, as shown in Figure 3-4(b) and the inset. We believe that the enlarged aspect ratio of CNT emitters and the decrease of the screen effect experienced by the individual CNTs in the emitter are attributed to the lower turn-on and threshold fields. It is well known that the turn-on electric field decreases as the length of CNTs increases [92]. Moreover, the density of CNTs on the circumference of the hemicylindrical structure decreases by increasing its radius as the clamping margin increases. The lower density of CNTs at the emitter might diminish the screen effect on field emission [93].

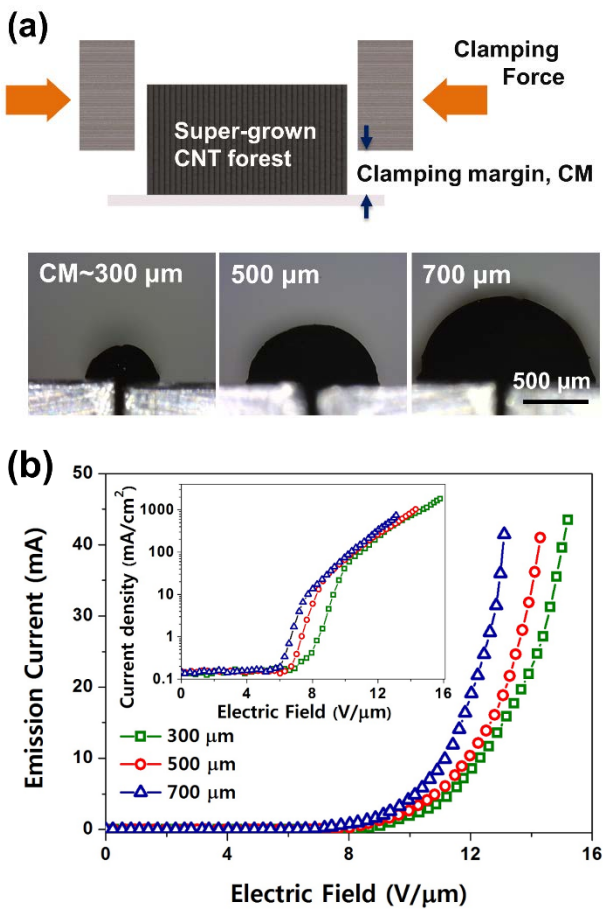

Figure 3-4. (a) Schematic and optic images of CNT line emitters with various radiuses by controlling clamping margin. (b) I-V plots of CNT line emitters with a radius from 300 to 700 μm. The inset shows plots of current density versus electric field.

As schematically described in Figure 3-5(a), the fabricated CNT line emitter has a hemicylindrical geometry and the CNTs radiate outward from the clamping edge. SEM image of emitter surface before treatment is shown in the upper panel. Although the midpoint of the emitter circumference has a minimum distance from an anode for field emission, the round shape emitter is not desirable for achieving high current density due to the broad distribution of the electric field along the circumference (Figure 3-6). Two types of post-treatment were carried out to improve the field emission performances of the CNT emitter. (1) First, we cut the “bread-shape” emitter out of both sides of a hemicylindrical CNT structure using a razor blade (see the left image of Figure 3-5(a)). (2) Second, a few drops of methanol were introduced to the surface of the hemicylindrical structure to make capillarity-induced densification of CNTs. On the liquid evaporation, van der Waals forces adhere to the adjacent CNTs, transforming them into patterned CNT needles with a high aspect ratio (see the SEM image in the right panel of Figure 3-5(a)). As shown in Figure 3-5(b), the post-treated emitters clearly show the enhanced field emission characteristics compared with the as-prepared CNT line emitter. The emitter prepared by liquid-densification shows the improved turn-on and threshold fields of 5.3 and 7 V/μm, and better improvements are achieved by the bread-shape emitter from 6.3 and 8.2 V/μm of the as-prepared emitter to 4.3 and 6.2 V/μm, respectively.

The stability of the field emission is of practical interest at a high current since the emitter can easily be damaged due to the oxidation of CNTs by Joule heating and ion bombardment of residual gases [94-96]. A long-term emission stability test was conducted, in which the electric field was maintained constant at the level corresponding to 10 mA for 10 hours. As shown in Figure 3-5(c), the current of the hemicylindrical CNT line emitter becomes degraded to a current level of ~9.2 mA, jagged with time. However, for the post-treated emitters, it is apparent that the currents are stabilized to ~10 mA with little fluctuation, showing better stability in a bread-shape emitter with on-time. The emission current density of 10 mA corresponds to approximately 625 mA/cm^2, based on the apparent emission area of the bread-shape emitter, which is about 0.016 cm^2

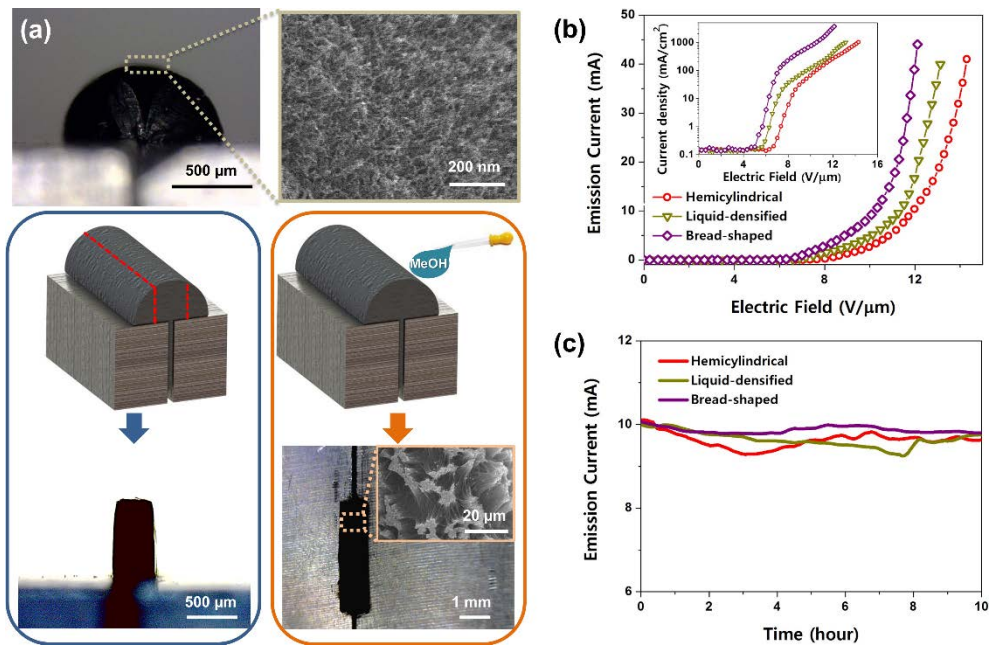

Figure 3-5. (a) Two types of post-treatment to improve field emission performance. (1) Bread-shape emitter by cutting the exterior of both sides using razor blade (the left image). (2) CNT needle emitter prepared by liquid densification (the right image). (b) I-V plots of post-treated emitters compared to the as-prepared CNT line emitter. The inset shows plots of current density versus electric field. (c) Emission stability tests of the emitters. The emitters were maintained constant at the level corresponding to 10 mA for 10 hours.

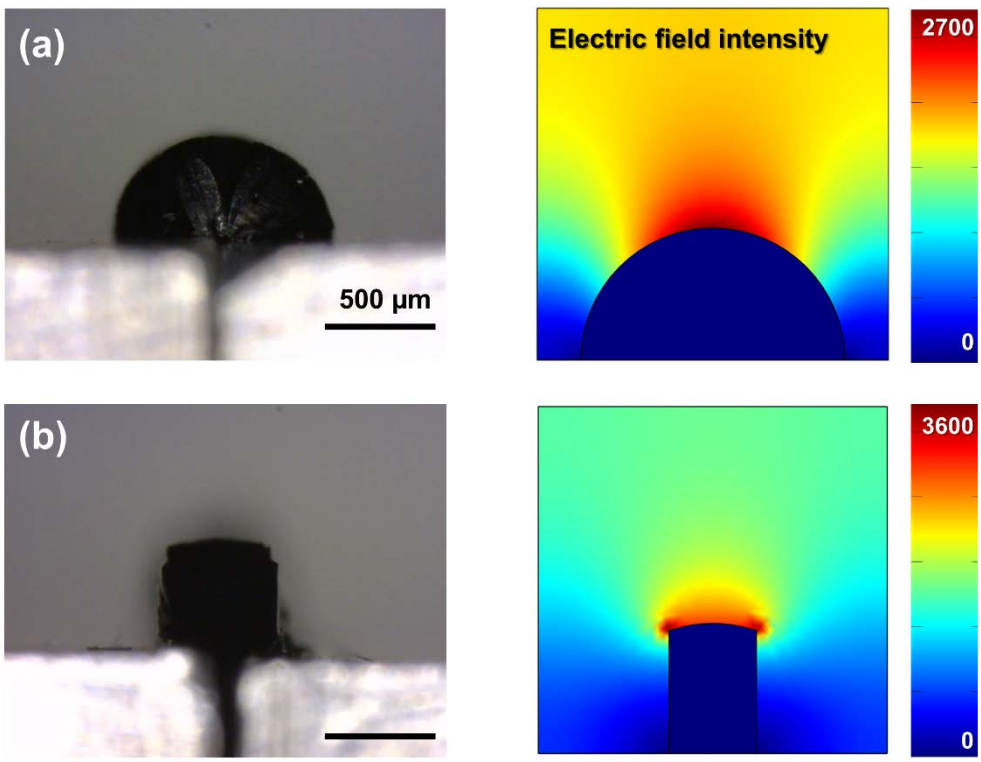

Figure 3-6. Optical images and electric field distribution of (a) hemicylindrical and (b) bread-shape emitters. Focusing an electric field caused by changing the geometry of CNT emitter might lead to the improvement in the field emission performances. The electric field was calculated by a commercially available program.

It is important to note that the present approach is highly scalable and productive as it does not involve any cumbersome process to manipulate intractable CNTs, such as dispersion, binder mixing, and patterning, etc [2, 34, 97, 98]. To demonstrate the scalability of the approach herein, we fabricated a CNT multi-emitter that can provide an extremely high current, prepared by clamping multiple CNT forests. Several structural and electrical parameters can significantly influence the field emission performance in a multi-emitter [99, 100]. Of these factors, making a uniform level of the emitters (i.e., leveling the height of the emitters) is an important criterion for superposing the best performance of each emitter. The multi-emitter composed of five bread-shape emitters (see the inset of Figure 3-7(a)) was fabricated by simultaneously clamping all the CNT forests in a single tongs, followed by cutting both sides of the hemicylindrical structures. In the present approach, the height of each emitter in the multi-emitter is solely determined by the clamping margin, without depending on the initial height of the CNT forests, so that the clamped CNTs have almost identical heights and geometries, even if the height of as-grown CNT forests might differ. As shown in Figure 3-7(a), the field emission current of the multi-emitter reached the maximum level of 103 mA (that is, the maximum level allowed by our power equipment) with a turn-on and threshold field of 4.8 and 6.4 V/μm, respectively. The emission stability of the multi-emitter was also tested in high emission current levels from 10 to

30 mA for 10 hours. As shown in Figure 3-7(b), very stable operations of the multi-emitter were observed with on-time, and the current degradation was negligible with little fluctuation. We believe that the remarkably high current level of 103 mA and emission stability of the multi-emitter could be attributed to the uniform geometric length of the emitters and the robust physical contact characteristics created by the mechanical clamping.

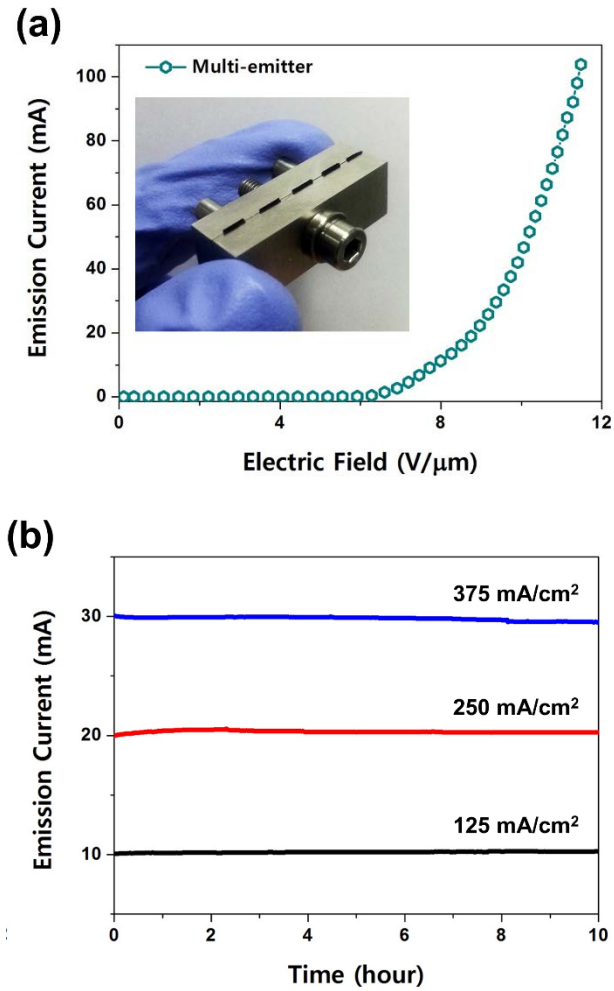

Figure 3-7. Multi-emitter composed of five bread-shape emitters and investigation of emission characteristics. (a) I-V plot of the multi-emitter. The inset shows optical image of the fabricated emitter. (b) Field emission stability tests of the multi-emitter with a constant current level of 10 to 30 mA.

3.4 Conclusion

We fabricated high-performance CNT line emitters using the macroscopic mechanical clamping process. By applying mechanical compression with a controlled clamping margin to a vertically aligned CNT forest, a hemicylindrical shape of CNT structure strongly held with the tongs electrode was achieved. With the robust mechanical, thermal, and electrical contacts created by the mechanical clamping process, the CNT line emitter, especially the bread-shaped emitter, showed superb field emission performance with an emission current of 43 mA, current density of 2700 mA/cm^2, and stable operation of over 10 hours. We also fabricated the CNT multi-emitter composed of five bread-shaped emitters. Excellent field emission performances, including an extremely high current of 103 mA and emission stability for 10 hours, were achieved, showing the significant applicability of the present emitter for high-power electron beam sources. Furthermore, the present approach is advantageous for a variety of applications, especially binder-free and high-performance CNT electrodes.

Chapter 4. Holey graphene film as a planar field emitter

In this work, we introduce an emitter in the shape of a hole, or hole emitter. To achieve high figure of merit and total current, we have investigated a new class of planar emitter with holey graphene film for negligible screening effect. An array of holes in graphene film can serve as a planar emitter, in which each circular hole is an emitter. Because of the nature of the sidewall emission through the edge of graphene film, the present planar emitter does not need any cumbersome process of leveling off emitter height and contriving to obtain the desirable inter-distance between emitters. Therefore, the screening effect and the field emission uniformity considered as obstacles in developing high efficiency planar emitters are easily resolved by an optimal design of the circular hole array. Moreover, the graphene film emitter is so flexible that it can be wrapped around a cylindrically shaped anode. This flexibility allows the present emitter to be used as a high power electron beam source because of the focusing of the emitted electron beams rendered by the concavely curved surface.

4.1 Background of planar emitter

With the superior field emission performance such as low turn-on voltage, high emission current density and long-term emission stability, electron field emissions based on graphene and its assembled structures have been extensively studied as an alternative to thermionic emission.[19, 30, 101] In particular, atomically sharp edges of graphene reduces greatly turn-on and applied voltages for electron emission owing to the amplification of field enhancement.[9, 22]

Field emitters can be divided into point and planar emitters, based on their geometry and relevant applications. The point emitters are preferred for applications in X-ray sources and electron beam instruments because of the small spot size for electron emission. Because of the high aspect ratio of point emitter, an applied electric field is strongly focused on the tip of the emitter. Accordingly, a judicious choice of material and its structural design are needed to tolerate the high current density and to prevent irreparable damage from Joule-heating for a stable and long-lasting operation with high performance.[102, 103]

Planar emitters have drawn interest for practical applications in field emission display. Chemical vapor deposition (CVD) growth of vertically aligned carbon nanotube and graphene sheet, coupled with the screen printing method,

is commonly employed to fabricate the planar emitters. All the emitters should have the same height to ensure uniform distribution of emission sites over the entire surface. Moreover, the field-screening effect caused by the proximity of neighboring emitters should be considered in the design of high efficiency planar emitters.[45, 104] The field-screening dominates the emission performance when the emitter is longer than the inter-emitter distance, resulting in a decrease in the emission current at a given applied voltage. A general design rule, according to a theoretical calculation, is to set the height of the emitters to approximately one half the inter-emitter distance to minimize the screening effect.[29, 105]

Planar emitters do not have the low current problem that the point emitter has due to its small emission area. Furthermore, the planar emitter, when made flexible, would enable generation of an extremely high density electron beam source by the aid of the beam focusing technique. This flexible planar emitter would widen the field emission applications to the electron beam source for Terahertz generator and the electron beam propulsion of spacecraft.

In this work, we introduce an emitter in the shape of a hole, or hole emitter. An array of holes in graphene film can serve as a planar emitter, in which each circular hole is an emitter. Because of the nature of the sidewall emission through the edge of graphene film, the present planar emitter does not need any cumbersome process of leveling off emitter height and contriving to

obtain the desirable inter-distance between emitters. Therefore, the screening effect and the field emission uniformity considered as obstacles in developing high efficiency planar emitters are easily resolved by an optimal design of the circular hole array. Moreover, the graphene film emitter is so flexible that it can be wrapped around a cylindrically shaped anode. This flexibility allows the present emitter to be used as a high power electron beam source because of the focusing of the emitted electron beams rendered by the concavely curved surface.

4.2 Result and discussion

Figure 4-1(a) illustrates schematically the field emission based on holey graphene film (HGF). The free-standing graphene film, approximately 110 nm thick, was fabricated by a specialized hydrothermal process followed by heat treatment at 1000 °C in Ar/H^2 environment. The graphene film has excellent physical (Young's Modulus: 92 GPa, Tensile Strength: 1700 MPa) and electrical (Conductivity: 4,900 S/cm) properties. Furthermore, it is flexible, and it can be handled with ease despite the small thickness of 110 nm (Figure 4-1(e)). The circular holes evenly formed on the graphene film were precisely patterned through a reactive ion etching (RIE) process. As

shown in the figure, the field emission property was measured (Figure 4-2) by applying a voltage between the two electrodes of Mo anode on the opposite side of HGF cathode.

The electric field intensity calculated by a commercially available simulation program is shown in Figure 4-1(b). An examination of the electric field distribution of the cross section of a circular hole (lower part of Figure 4-1(a)) reveals that the electric field intensity is two orders of magnitude higher than that of graphene film without circular holes (upper part of Figure 4-1(b)). The electric field is concentrated intensely along the circumference of the circular holes on the graphene film. Therefore, uniform emission performance is facilitated even without a leveling process for each emitter (circular hole).

The scanning electron micrograph (SEM) image of patterned graphene film is shown in Figure 4-1(c). The circular hole array was isotropically etched using a metal mask with circular holes through an oxygen plasma RIE. With the aid of the metal mask, the diameter and intervals of circular holes can be designed and a large-area patterning is possible. The graphene film is physically strong and remains free-standing even after the RIE as shown in Figure 4-1(d).

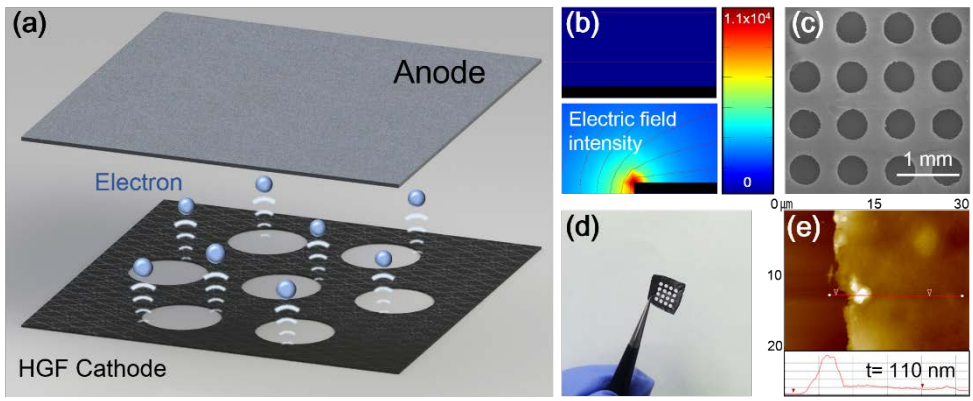

Figure 4-1. (a) Schematic illustration of field emission using HGF. (b) Electric field intensity calculated by a commercially available simulation program without circular hole (upper part) and with the circular hole (lower part). (c) SEM image of the HGF with 500 ㎛ hole array. (d) Optical image of the freestanding HGF after RIE etching process. (e) AFM image of graphene film, showing the thickness to be 110 nm.

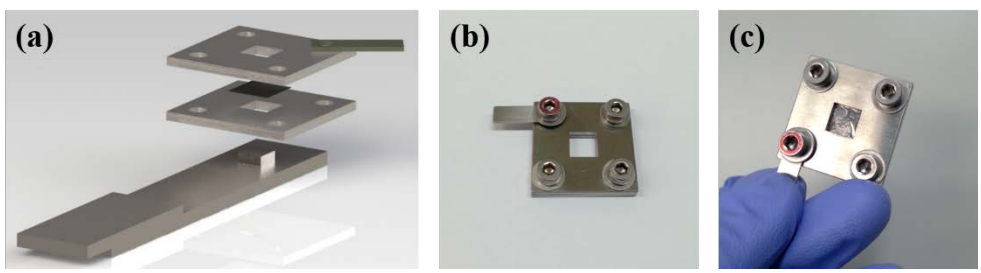

Figure 4-2. (a) Schematic illustration of field emission setup using HGF. (b) Optical image of the zig for holding the HGF. (c) Optical image of the zig after loading the graphene film.

To improve the electrical conductivity of the graphene film fabricated by the hydrothermal process, the film was heat-treated. The corresponding change in the sheet resistance is shown in Figure 4-3(a) as a function of the temperature. The sheet resistance was reduced partially during the hydrothermal process to approximately 1,400 Ω/□. This resistance can be reduced further by removing the residual oxygen functional groups (epoxy, hydroxyl, carboxyl groups) through the heat treatment. By performing the heat treatment at 1,000 °C in Ar/H^2 (30 sccm: 15 sccm), the sheet resistance was decreased by two orders of magnitude. The Raman spectra of the graphene film are shown in the inset of Figure 4-3(a). As the heat treatment temperature was increased, the D(~1350 cm^{-1})/G (~1580 cm^{-1}) ratio increased slightly. At still higher temperatures, more residual oxygen functional groups are removed and the D-peak increases further.[106, 107] An optical image of a hole etched through the graphene film is shown in Figure 4-3(b). The enlarged image in the inset reveals that there are many protruding graphene sheets with sharp tips and edges along the circumference of the circular holes. These protruding features of HGF offer great advantages for excellent field emission performance.[108]

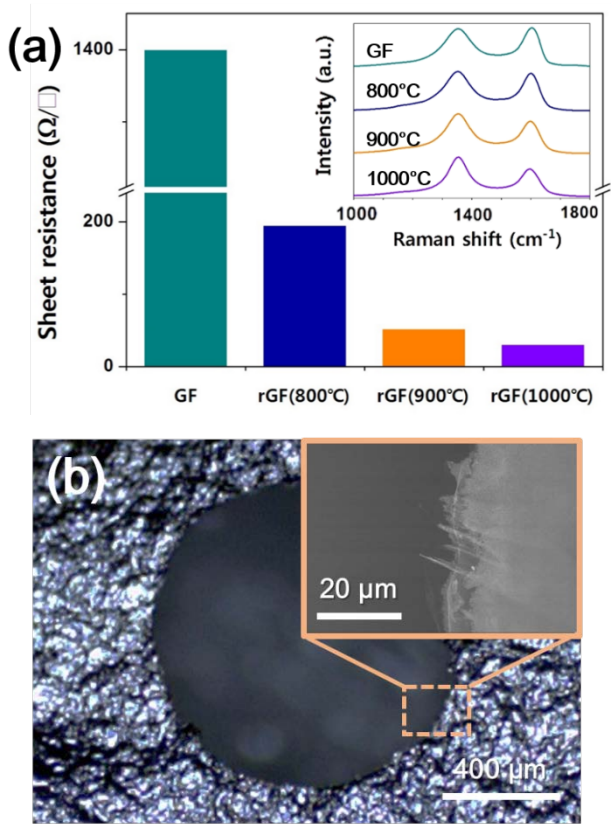

Figure 4-3. (a) Change of sheet resistance and Raman spectrum of graphene film (GF) with heat treatment temperature (rGF = reduced GF). (b) Optical image of holey graphene film (HGF), showing a hole obtained by RIE etching process. The inset shows an SEM image of protruding graphene sheet edges along the circumference of the circular hole.

The field emission performance of an emitter is largely determined by the density of emitters and the screening effect between emitters. To achieve a high current density, many emitters per unit area have to be fabricated. On the other hand, a rapid decrease in the electric field produced between neighboring emitters by the screening effect induces performance degradation of all field emitters.[29, 45, 104, 105] In the case of the conventional field emitter with one-dimensional structure of high aspect ratio, the emitter's height and the inter-emitter distance determine the screening effect.[29, 105] In the case of the HGF, however, both the screening effect occurring in a single circular hole and the screening effect occurring between many circular holes have to be considered.

Figure 4-4(a) shows the current density as affected by the hole size in the graphene film, with the film with no hole as the reference. When there is no circular hole, almost no field emission occurs because of the absence of the electric field concentration. With the presence of holes, on the other hand, an enhanced field emission performance results because the electrons are well emitted by the electric field concentrated along the circumference of the circular holes. In fact, the current density increases as the diameter of the circular hole increases for the same electric field (Figure 4-4(a)). As the diameter of circular hole increases, so does the emission site area and the screening effect decreases.

The line plot in Figure 4-4(b) shows the field enhancement factor (β) calculated by a commercially available simulation program as a function of the hole size. The field enhancement factor is given by

$$\beta = E_{local}/E_0 \quad (1)$$

where E_{local} is the local electric field at the emitter surface and E_0 is the applied electric field.[33, 71] The simulation result given by a line in the figure shows that the enhancement factor increases rapidly with the hole size and then reaches a plateau as the hole size reaches 2 mm. The experimental values given by dots in the figure also show a trend similar to the simulation result. The screening factor (α) derived through the field enhancement factor is given by

$$\beta_x = \beta_0(1 - \alpha) \quad (2)$$

$$\alpha = \exp(-0.0021\mathrm{x}) \quad (3)$$

where β_x is the field enhancement factor for the circular hole size x, and β_0 is the field enhancement factor without screening effect. The screening factor decreases exponentially with the circular hole size as shown in the figure, similar to the screening factor of the conventional field emitter.[29, 105]

The current density as affected by the number of holes for a fixed hole size is given in Figure 4-4(c) as a function of the electric field. The experimental results in the figure show that the current density increases with increasing number of the holes for the same electric field. The field enhancement factor

given in Figure 4-4(d) for both simulation (line plot) and experiment (dot plot), however, reveals that it is independent of the number of holes, which implies that the screening effect between the circular holes is absent. Therefore, the enhanced field emission performance shown in Figure 4-4(c) was the result of an increase in the emission area.

Two major differences distinguish the HGF emitter presented here from the conventional field emitter that is based on an 1D structure with high aspect ratio. In the first place, there is no dependence of the screening effect on the distance between emitters. In the conventional field emitter, on the other hand, the screening effect does depend on the separation between emitters unless they are separated by more than or equal to twice the 1D structure's height.[29, 105, 109, 110] Consequently, the electric field intensity decreases due to the screening effect when the density of the emitters is high. In contrast, the emitter density of the HGF can be increased by integrating the circular holes without worrying about the decrease in the field intensity due to the absence of the screening effect. In the second place, there is no need for leveling the height of emitters. In the conventional emitter, however, an additional height leveling process such as electric discharge machining (EDM), electrical treatment, and chemical etching is needed after 1D structure arrangement.[111-113] If the height of emitters is not uniform, damages to the emitters occur due to the excessive concentration of the local field, and an unstable field emission

results. In contrast, high-performance HGF field emitters can be produced without height leveling because the circular holes are on a flat graphene film.

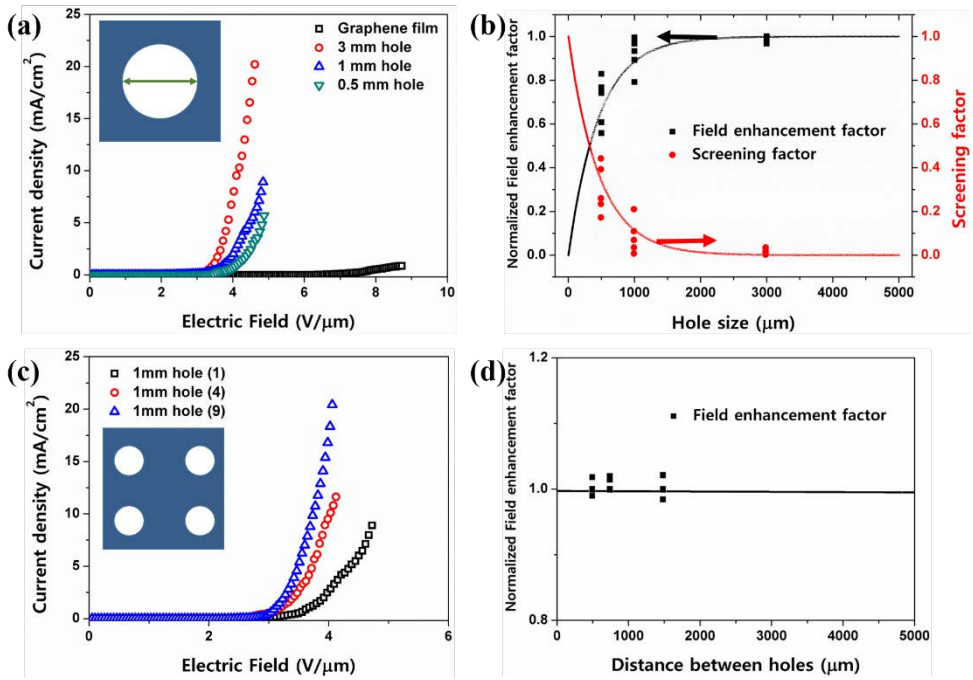

Figure 4-4. (a) I-V plots of pristine graphene film and HGF with hole diameter ranging from 500 to 3000 ㎛. The inset shows the geometry of the HGF. (b) Field enhancement factor and screening factor of the HGF as a function of the hole size: simulation value (line plot) and experimental value (dot plot). (c) I-V plots of HGF for various number of circular holes. The inset shows the geometry of the multi-hole HGF. (d) Field enhancement factor of the multi-hole HGF as a function of the distance between the holes: simulation value (line plot) and experimental value (dot plot).

For an optimal integration of the circular holes, we utilize the emission current described by the Fowler-Nordheim equation:[114, 115]

$$I = Aa\varphi^{-1}E_{local}{}^{2}\exp(-b\varphi^{3/2}/E_{local}) \quad (4)$$

where I is the emission current, A is the emission area of the field emitter, φ is the work function of the graphene, A and B are the Fowler-Nordheim constants given by $1.56 \times 10^{-6}A \cdot V^{-2}eV, 6.83 \times 10^{7}V \cdot eV^{-\frac{3}{2}}cm^{-1}$. Figure 4-5(a) shows the simulation result of the normalized emission current based on the Fowler-Nordheim equation as a function of the hole size or diameter for a graphene film with an area of 1cm^2 and a thickness of 100 nm. As shown in the figure, a maximum exists with respect to the hole size. The optimal value of 1600 μm for the size is the result of the tradeoff between the emission area and the field enhancement factor. As the circular hole size increases, the field enhancement factor also increases but the emission area decreases because a smaller number of holes can occupy a given HGF area.

On the basis of the optimal value (circular hole size=1600 μm) in Figure 4-5(a), which allows for 16 holes for the given area of 1cm^2, the HGF emitters were fabricated. Figure 4-5(b) shows that the fabricated HGF emitters can deliver a low turn-on field of 1.8 V/μm (current density of 10 μA/cm^2), a threshold field of 2.4 V/μm (current density of 1 mA/cm^2) and a high current density of 40 mA/cm^2 at 3.8 V/um. These values represent the HGF emitter

performance that is far better than the conventional planar field emitters (Figure 4-6).[15, 20, 22, 29, 116-121]

Another distinct feature of the HGF emitter is its stability. Figure 4-5(c) shows that the HGF emitter can maintain high current densities of 10 and 20 mA/cm^2 stably for 120 hours. Such a stability at the high current densities could be due to the uniform height of the emitter and excellent properties of the graphene film. The flexible nature of the holey graphene film should enable shaping of electron beams through the manipulation of the emission area. The result shown in Figure 4-5(d) (Figure 4-7) demonstrates the point, where excellent field emission performance is confirmed at the curvature radius of 1.5 mm.

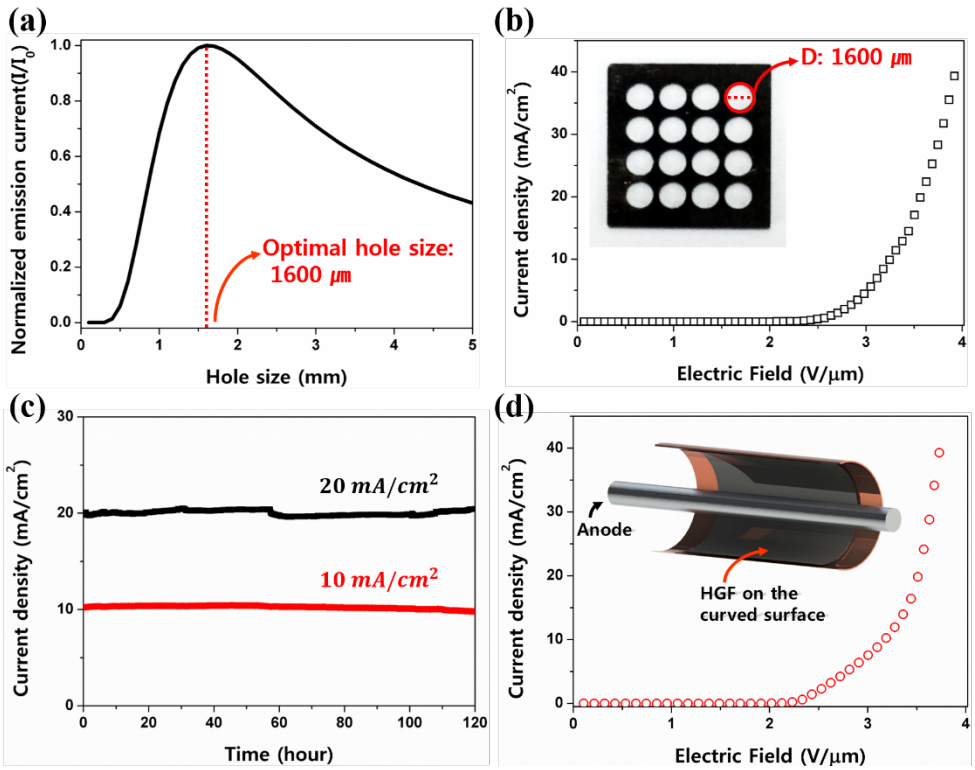

Figure 4-5. (a) The normalized emission current as a function of the hole size for the optimal design of HGF. (b) I-V plots of HGF with a diameter of 1600 ㎛. The inset shows optic image of the HGF. (c) Field emission stability tests of the HGF with a constant current density level of 10 and 20 mA/cm^2 for 120 hours. (d) I-V plots of HGF with a curvature radius of 1.5 mm. The inset shows schematic illustrating of the flexible field emitter for focused electron beam.

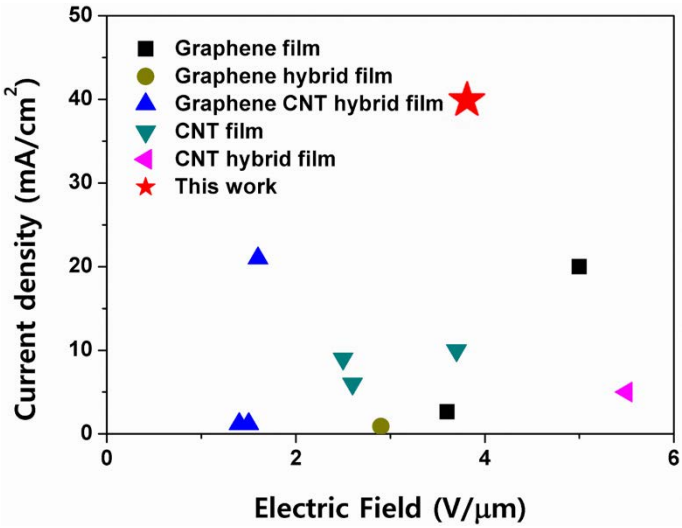

Figure 4-6. Performance comparison of this work with other planar emitters fabricated by various structures such as graphene film, graphene hybrid film, graphene CNT hybrid film, CNT film, CNT hybrid film.[15, 20, 22, 29, 116-121] The HGF planar emitter shows an outstanding performance with a high current density of 40 mA/cm^2 at 3.8 V/um compared with the previously reported emitters.

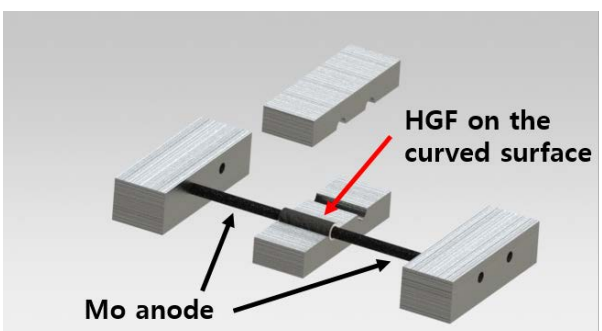

Figure 4-7. Schematic illustration of flexible field emission setup using HGF for focused electron beam.

4.3 Conclusion

In summary, a new class of planar emitter has been introduced that outperforms by far the conventional planar emitter. An array of holes etched through a graphene film constitutes the holey planar emitter. In this emitter, the applied electric field is concentrated on the edge along the circumference of each hole and the edge of graphene film provides efficient field emission sites with a great amplification of field enhancement. The optimal hole size and the number of holes for a given film area can be obtained with the aid of Fowler-Nordheim equation. Unlike the conventional planar emitter, there is no dependence of the screening effect on the distance between emitters and neither is there a need for leveling the height of emitters because of the nature of the holey graphene film (HGF). Another distinct feature of the HGF emitter is its stability with time at high current density. The flexible nature of the HGF should be advantageous for a variety of applications, especially for flexible high-power electron beam source that can be obtained by focusing high-density electron beams.

Chapter 5. Carbonized cork emitter for multidimensional field emission

To broaden the range of application of electron beams, low power field emitters are needed that are miniature and light. We introduce here carbonized cork as a material for field emitters. To achieve high figure of merit and high current, we have investigated the uniform hexagonal honeycomb structure of cork for high field enhancement factor and negligible screening effect. The light natural cork becomes graphitic honeycomb upon carbonization, with the honeycomb cell walls 100-200 nm thick and the aspect ratio larger than 100, providing an ideal structure for the field electron emission. Compared to nanocarbon field emitters, the cork emitter produces a high current density and long-term stability with a low turn-on field. The nature of cork material makes it quite simple to fabricate the emitter. Furthermore, any desired shape of emitter tailored for the final application can easily be prepared for point, line, or planar emission.

5.1 Background of low turn-on field emitter

Electron beams are widely employed in various applications, including X-ray photography and computed tomography (CT) scans in hospitals, fault detection of semiconductor devices, airport security, and terahertz generation.[1-3] Moreover, electron beam generators are progressively becoming more miniaturized, light-weighted, and low-powered so that they can be applied to diverse areas.

Although thermionic emission, an emission resulting from heating a source to a high temperature, is the most common way of generating an electron beam, it is yet to overcome disadvantages such as high power consumption, complicated structure, and difficulty in operation.[4, 5] Carbon-based nano-materials have been utilized to relieve these limitations. With excellent mechanical, electrical, and thermal properties of these carbon-based materials, and their natural sharp edges that are highly suitable for focusing electric fields, excellent field-emission performance should result such as low turn-on electric field, high emission current density, and long-term stability.[6-8] In particular, graphene, a two-dimensional sheet consisting of sp^2-hybridized carbon atoms, is receiving much attention due to its superior electric field enhancement capability, originating from the atomically sharp edges of its layered structure.[9, 10]

Various methods have been developed to form a graphene structure that is suitable for field emission such as direct growth, electrophoretic deposition (EPD), ion-mediated assembly (IMA), spin coating, screen printing, and transfer processes.[11-24] These methods, however, require a high-temperature chemical vapor deposition (CVD) process, a complicated oxidation process to make the graphene oxide solution, or a cumbersome transfer process which makes fabrication very difficult. The graphene sheets in the graphene structure fabricated by these methods are usually randomly oriented and the protruding graphene sheets cause a local concentration of electric field, leading to excessive field emissions and eventually destruction due to Joule heating.[25, 26] Presence of randomly oriented dense graphene sheets, on the other hand, decreases the electric field due to screening effect,[27-29] resulting in an inefficient electric field distribution and hence imposing a limit on the field emission enhancement.

In this work, we introduce carbonized cork (C-cork) as a high-performance field emitter. Pristine cork (P-cork), a protective tissue of plants formed around the peripheries of the stems or roots, exhibits a highly organized structure with pores of several tens of micrometer size evenly arranged. This highly organized structure is optimal for a field emitter because it allows for uniform concentration of electric fields. A carbonization process can transform the cork into the C-cork with graphitic sheet. We utilize this C-cork

as a material for mass-producing the field emitter in one single step. A high-performance, low-power field emitter that can be manufactured in various forms is developed using the natural organic material, cork.

5.2 Experimental section

Cork is a protective tissue that grows between the outer and inner bark of cork oak trees with a highly organized structural arrangement. Cork comprises 42 million cells per cubic centimeter, and the cell walls form a hexagonal honeycomb structure. The cell walls of the cork consist of suberin, lignin, and cellulose, and are approximately 1–2 μm thick. If the cork is heated to 1000 °C in argon gas, the organic substances of the cell walls are converted into a polyaromatic carbon material as a result of the carbonization,[122] resulting in carbonized cork or C-cork. During the carbonization process, the 1–2 μm cork cell walls become graphitic sheets approximately 100–200 nm thick, acquiring a high aspect ratio (~133).

To fabricate various emitters, the P-cork was first cut into 500 ㎛ thick disks using a microtome (MICROM Lab, HM 340 E), and this P-cork disk was converted to C-cork disk by carbonization. For the planar emitter, four sides of the C-cork disk were cut and the flat rectangular surface was used as the emission site. For the line emitter, a narrow block was made by cutting the

disk and the upper surface in stripe shape was used as the emission site. For the point emitter, the edges of a square pillar- shaped C-cork was ground to form a pointed end for the emission site (Figure 5-1).

The field emission characteristics were measured under 3.0 x 10^{-7} Torr. A voltage between C-cork cathode and a metal anode (Molybnedum) was applied using a DC power supply (Matsusada Precision Inc.). The emission current was measured using a multimeter (Keithley 2000). This emission current was divided by the apparent area of emission plane to obtain the current density (Figure 5-1). The electrical conductivity of C-cork was measured using a 4 point probe (Changmin, FPP-5000). Scanning electron microscopy (SEM) analysis was performed using a Hitachi S-4800 field emission electron microscope at an acceleration voltage of 10-15 KeV. X-ray photoemission (XPS) experiments were carried out by using a XPS spectrometer (Kratos, AXIS-HSi). The Raman spectra were measured using a micro-Raman system (JY-Horiba, LabRam 300) with excitation wavelength of 532 nm. Thermo-gravimetric analysis (TGA) was carried out under air environment with a thermo-gravimetric analyzer (Discovery TGA, TA Instruments) at a heating rate of 10 °C min^{-1}. High resolution transmission electron microscopy (HRTEM) is used to image the structure of C-cork. The HRTEM study was carried out using a JEM-3010(JEOL Ltd, Japan). Prior to observation, TEM grids were prepared as following: the C-cork was finely

crushed, then dispersed in N,N-Dimethylformamide(DMF) using sonication for 4h. A droplet of the obtained suspension was deposited on a copper grid and dried.

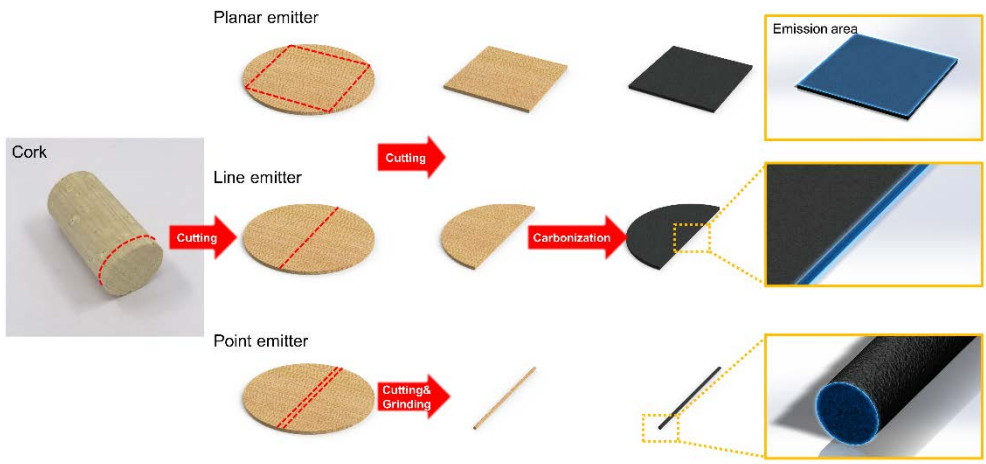

Figure 5-1. Schematic illustration of fabrication process.

5.3 Result and discussion

Field emission involves tunneling of electrons from the surface of a solid into a vacuum, under the influence of an external electric field.[70-72] Therefore, a structure that allows easy transfer of electrons and strong focus of the electric field is suitable for field emission. The scheme of field emission by the C-cork is illustrated in Figure 5-2(a). Each of the vertically oriented graphitic sheets serve as an excellent field emission site and emits electrons into the vacuum. Because the graphitic sheets are a single structure formed by the growth of tree, all graphitic sheets are well interconnected without any contact resistance, allowing for the favorable movement of electrons and efficient field emission.

The electric field intensity at the emission site was analyzed using a commercial simulation program (Figure 5-2(b)). The result shows that the electric field is highly focused at the top and edge of the graphitic sheets. Figure 5-3 reveals the dependence of the field enhancement factor (β) on the distance between emitters as estimated from electrostatic calculations.[27-29] The field enhancement factor indicates a degree of electric field enhancement due to the field emitter's geometric effect. As shown in the figure, the field enhancement effect diminish rapidly, due to the screening effect, for distances between emitters less than 20 ㎛ for the given height of 20 ㎛. Due to the

uniform hexagonal honeycomb structure of C-cork, approximately 30 μm in size, the screening effect of C-cork is negligible. Therefore, the field emission performance benefits from a highly regular structure that does not cause the screening effect.

Physical changes that occur due to the carbonization were examined with a P-cork sectioned to a thickness of 500 μm. Figure 5-2(c) shows that the brownish P-cork became black upon carbonization but still maintains its original form without any physical damage or deformation. Therefore, any desired shape of C-cork can be prepared by simply shaping the P-cork as desired (Figure 5-1). This feature is highly advantageous for the manufacture of field emitters with the shape tailored for targeted electron beams (Figure 5-4). Figure 5-2(d) reveals the changes that occur to the cork walls when the cork is carbonized. As shown, the graphitic sheets became transparent due to the carbonization, allowing the lower layers of the graphitic sheets to be observed, thus revealing a uniformly organized structure. The enlarged SEM image shows that the fabricated graphitic sheet has sharp edges 100-200 nm thick and very flat surface. The cutting plane of cork was chosen in such a way that the walls of honeycomb cell lie in parallel to the applied field to induce a local enhancement of electric field.

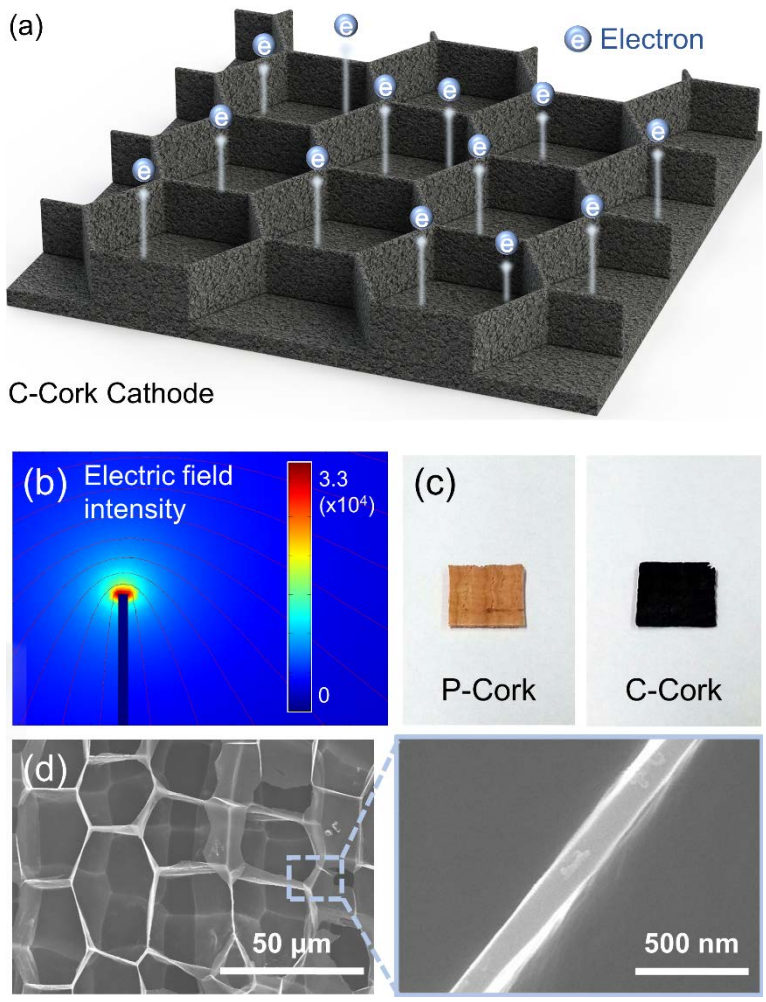

Figure 5-2. Field emission mechanism and structure of C-cork. (a) Schematic illustration of field emission from C-cork. (b) Simulated electric field intensity at the graphitic sheet. (c) Optical image of cork before (P-cork) and after carbonization (C-cork). (d) Scanning electron microscope (SEM) images of C-cork.

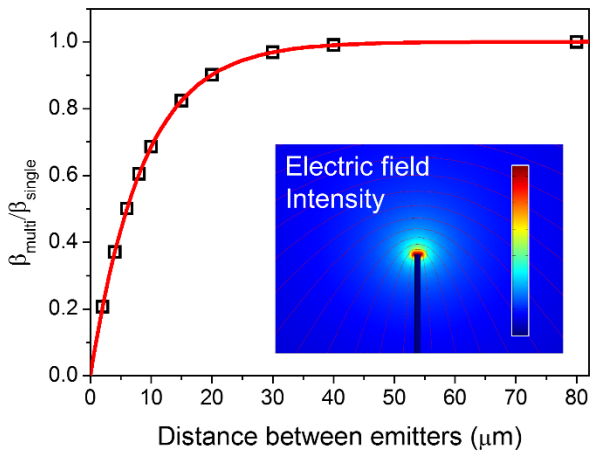

Figure 5-3. Dependence of the field enhancement factor of C-cork with multi emitter (β_{multi}) and single emitter (β_{single}) on the distance between emitters as estimated from electrostatic calculations.

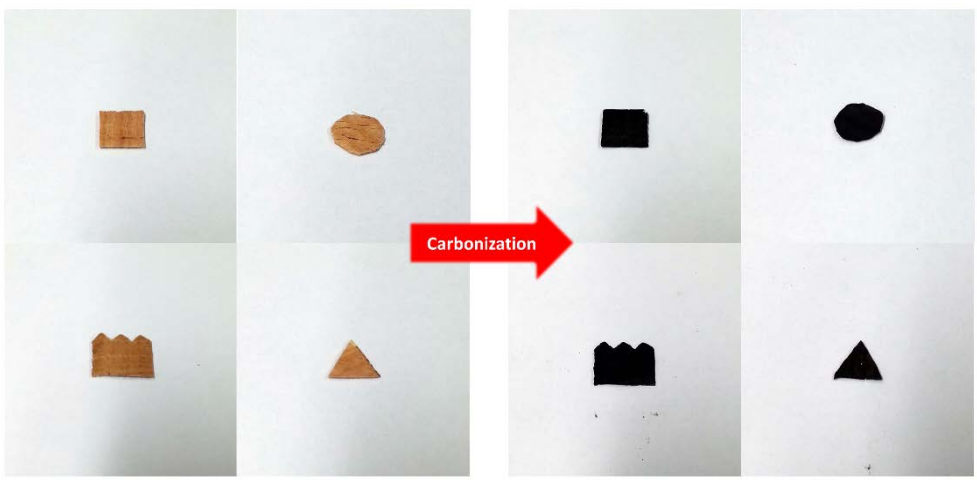

Figure 5-4. Optical images of cork in various forms before and after carbonization.

The physical change in the cork is highlighted in Figure 5-5. The P-cork shows opaque, thick cell walls, approximately 1–2 μm thick, with large wrinkles. On the other hand, the C-cork carbonized at 1000 °C shows similarly sized pores as before the carbonization but thinner cell walls 100-200 nm thick that have been converted to graphitic sheets. Thinning of the graphitic sheets occur due to pyrolysis of the contaminants and carbonization of the organic substances during the heat treatment. Even when the carbonization temperature is lowered to 800 °C, the graphitic sheets form well (Figure 5-6).

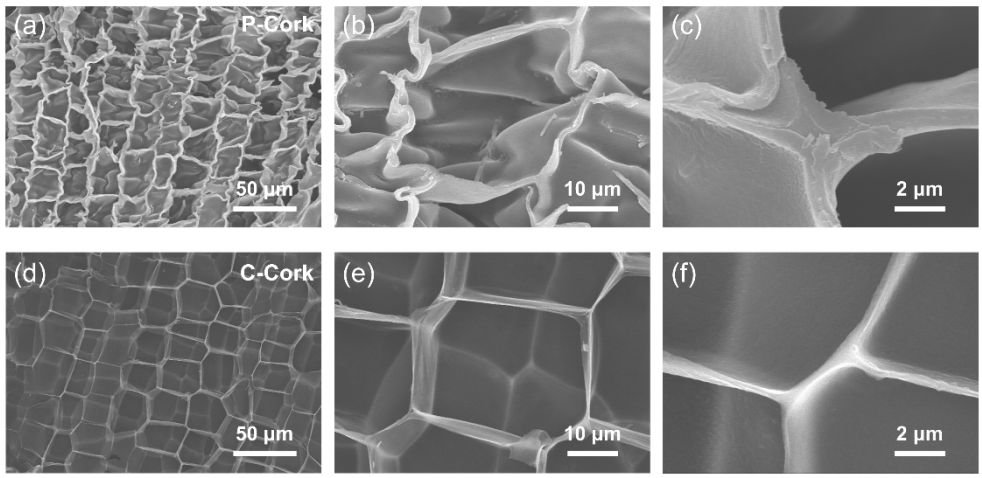

Figure 5-5. Physical changes in cork structure accompanying carbonization. (a-c) Low- and high-resolution SEM images of P-cork. (d-f) Low- and high-resolution SEM images of C-cork.

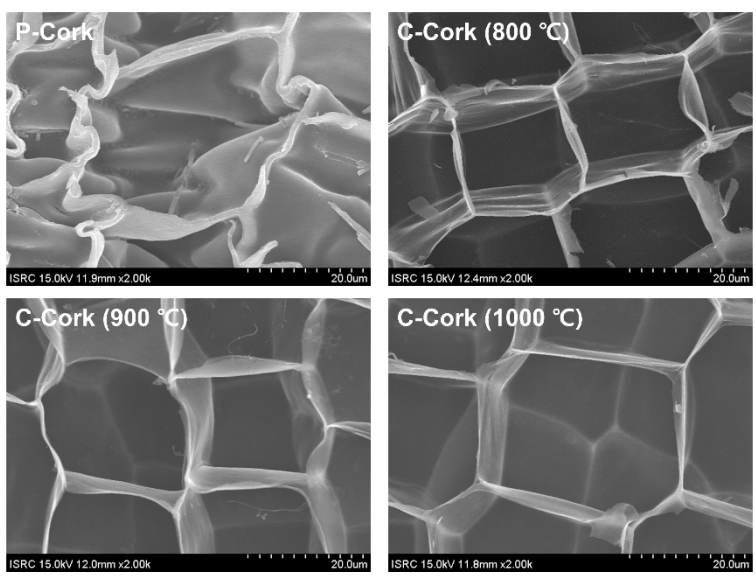

Figure 5-6. SEM images of P-cork and C-cork with various carbonization temperature.

To ascertain whether the cork walls convert to graphitic sheets upon carbonization at 1000 °C, XPS analyses were conducted for both P-cork (Figure 5-7(a)) and C-cork (after carbonization, Figure 5-7(b)). The results for the C-cork show that among the major peaks of the P-cork, the C-O-C (epoxy/alkoxy) bond at 286.6 eV became greatly weakened, whereas the C-C bond at 284.6 eV remained the same, an indication that a large number of the epoxy and alkoxy groups in the P-cork were effectively removed during the carbonization process.[123, 124] Both the C-OH (alcohol) bond at 285.6 eV and the C=O (carbonyl) bond at 288.4 eV were also shown to be greatly reduced. Another instrumental method used was Raman spectroscopy. As shown in Figure 5-7(c), D- and G-peaks appear after the carbonization (C-cork) that were absent in the case of the P-cork. Furthermore, the intensity ratio of the D to G band is shown to progressively increase from 0.85 to 0.90 with increasing carbonization temperature, indicating that as the carbonization temperature increases, more oxygen functional groups of the P-cork are removed at higher temperatures.[106, 125] The electrical conductivities determined for both P-cork and C-cork (Figure 5-7(d)) reveal that the P-cork is an insulator whereas the C-cork is a conductor. The C-cork conductivity increases with increasing temperature, which indicates that the oxygen functional groups, which hinder electron movement, are successfully removed.[106, 126] As XPS and Raman do not clearly define whether the C-cork

is graphitic carbon or amorphous carbon, a thermo-gravimetric analysis was also carried out as shown in Figure 5-7(e). Given the oxidation temperatures of amorphous carbon and graphitic carbon,[127-131] C-cork carbonized at 1000 °C is expected to have a structure between amorphous carbon and graphitic carbon, similar to the results reported earlier on the carbonization of wood.[132, 133] The crystalline property of C-cork was investigated by high-resolution transmission electron microscopy (HRTEM). As shown in Figure 5-7(f) and Figure 5-8, C-cork is comprised of amorphous domains and short-range graphitic domains, which agrees with the result of TGA. The average interlayer spacing of graphitic domain was ~0.343 nm, which is slightly larger than that of pure graphite (0.335 nm), implying the turbostratic stacking in C-cork. [134, 135]

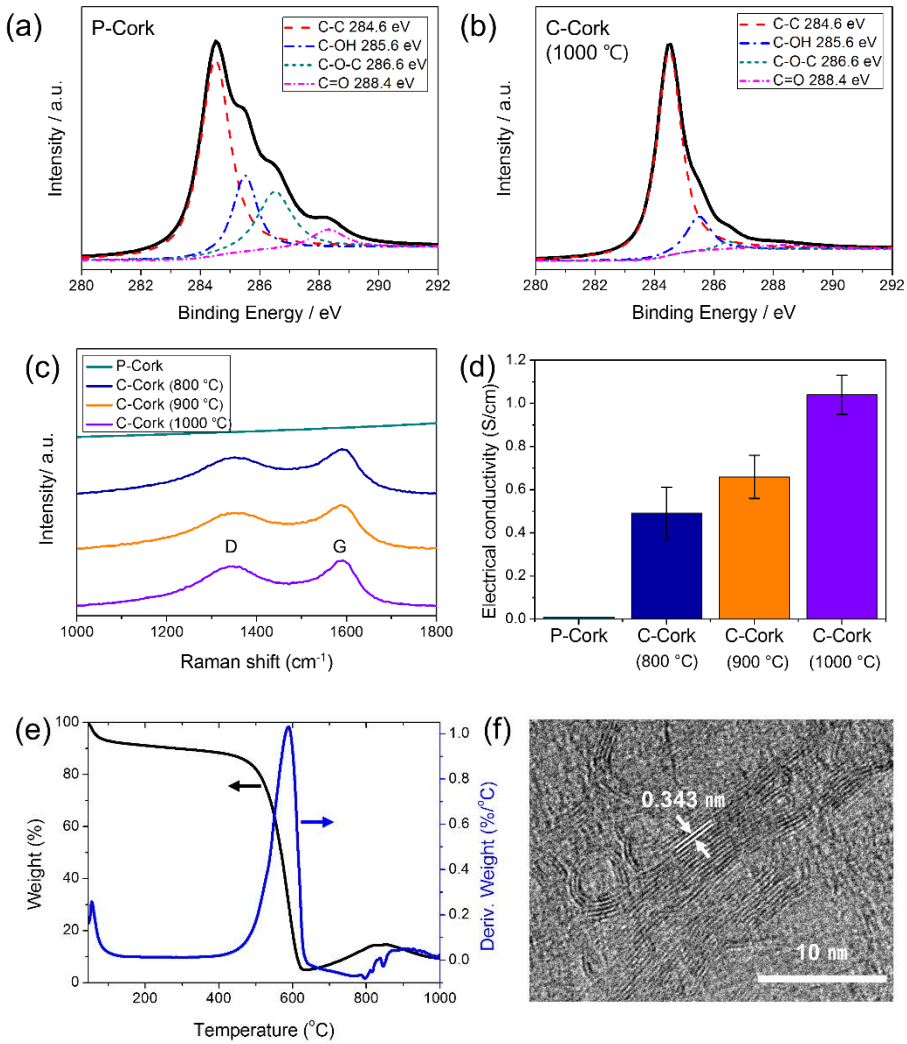

Figure 5-7. Graphitic nature of carbonized cork. (a-b) XPS spectra before (P-cork) and after carbonization (C-cork), respectively. (c) Raman spectra, (d) Electrical conductivity of P-cork and those of C-cork at various carbonization temperatures. (e) Thermo-gravimetric analysis, (f) HRTEM images of C-cork carbonized at 1000 °C

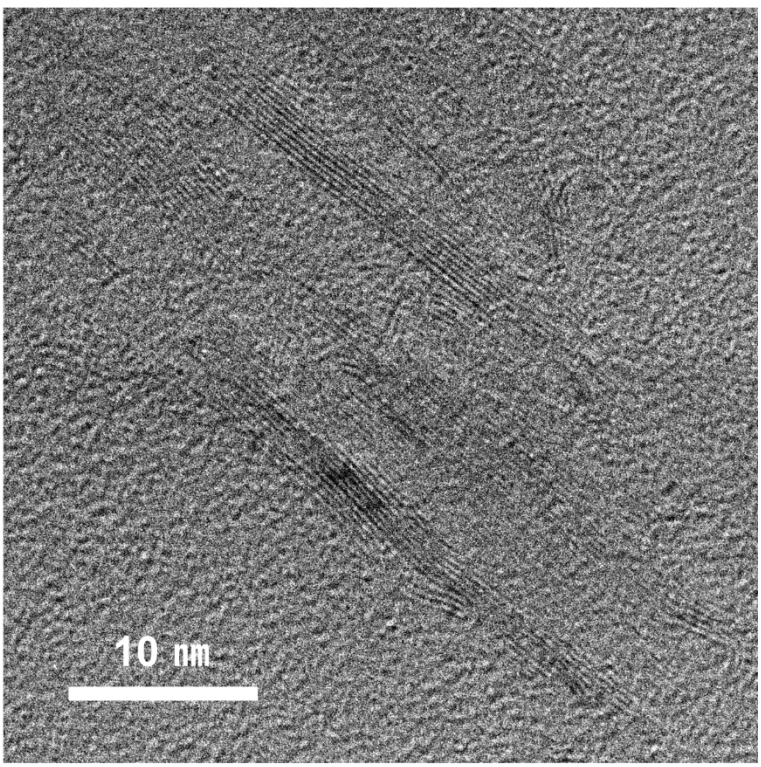

Figure 5-8. HRTEM images of C-cork carbonized at 1000 °C.

With the confirmation, field emission experiments were conducted using the C-cork carbonized at 1000 °C. The C-cork was physically robust and free-standing, allowing for easy scaling-up, as shown in Figure 5-9(a), (c). The flat surface of the C-cork, approximately 1 cm^2 in area, was used as the emission site for the planar emitter. The edge of the C-cork, approximately 500 μm thick, was used as the emission site for the line emitter. The setup used for the field emission performance of the C-cork emitters is illustrated in Figure 5-9(a), (c).

The experiments were carried out in a vacuum chamber at a base pressure of 3.0 x 10^{-7} Torr. The C-cork tightly compressed in the slot between two stainless steel jigs is the cathode as shown in Figure 5-10. A voltage was applied and the current flow between the cathode and anode was measured.

Figure 5-9(b) shows that the C-cork planar emitter provides a high maximum current density of 70 $mAcm^{-2}$. A long term stability with 10 and 30 $mAcm^{-2}$ is also demonstrated in the figure. Figure 5-9(d) displays the performance of the C-cork line emitter, showing a low turn-on field (electric field needed to produce a current density of 10 μAcm^{-2}) of 0.93 V μm^{-1} as well as a high maximum current density of 41 $mAcm^{-2}$. The low turn-on field of C-cork line emitter can be attributed to the edge that constitutes the line emitter, which could focus the electric field, compared to the planar emitter.

Compared to those previous nanocarbon field emitters, the field emission characteristics exhibit a very low turn-on field and a high maximum current density. This excellent field emission performance is attributed to the vertical graphitic sheets with sharp edges 100–200 nm thick.

The walls of honeycomb cell on the edge of the C-cork are vertical, inducing a local enhancement of strong electric field (see the cross-sectional SEM images of C-cork line emitter in Figure 5-11).

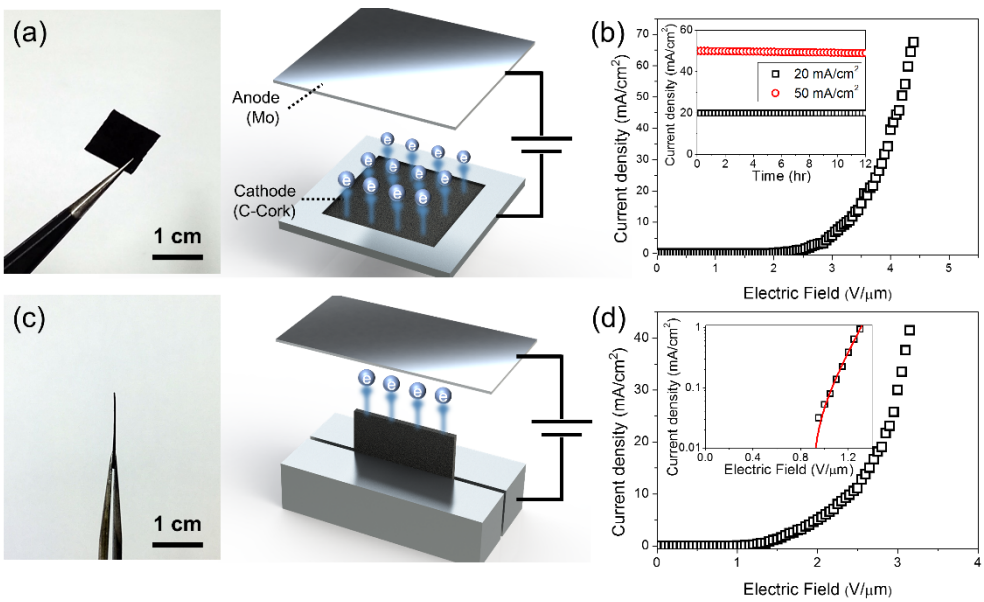

Figure 5-9. Photographs of emitter and field emission performance of C-cork. Optical front (a) and side (c) images of C-cork. Schematic illustrations of planar and line emitter, emitting electrons from the C-cork surface, along with the field emission performance of C-cork planar (b) and line (d) emitter respectively.

Figure 5-10. Setup for field emission test of line and planar emitter. The molybdenum anode is at the bottom, and the stainless steel jig is used for compressing the cork for C-cork line and planar emitter.

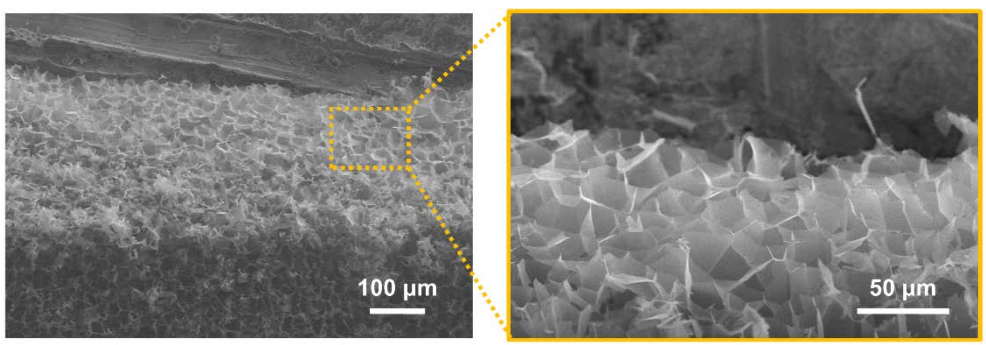

Figure 5-11. Cross-sectional SEM images of C-cork line emitter.

High aspect ratio of 133 of the graphitic sheet, approximately 20 μm in height, induced a local enhancement of strong electric fields. Furthermore, there was almost no screening effect, which occurs when emitters are excessively dense, because the graphitic sheets were spaced out from one another by 30 μm due to the pores that are naturally produced through the tree's growth and development.

In essence, the outstanding field emission performance of C-cork is achieved by negligible screening effect due to the uniform hexagonal honeycomb structure and the completely continuous graphitic sheet structure with high aspect ratio without any contact resistance (a cross-sectional SEM image of C-cork is shown in Figure 5-12).

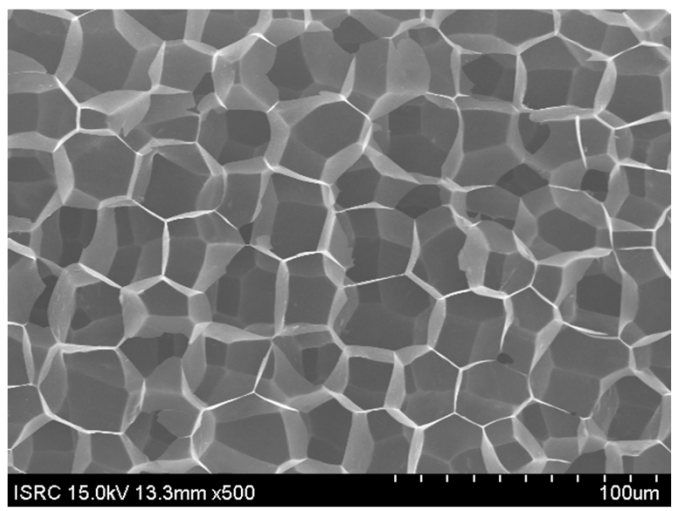

Figure 5-12. Cross-sectional SEM image of C-cork.

A point emitter was also fabricated by mechanically grinding the C-cork, using a fiber that is 250 μm in diameter (Figure 5-13(a)). Because C-cork is similar to pencil lead, it can be easily shaped into various forms through the repetitive mechanical grinding. Even after the mechanical processing, the graphitic sheets maintained their original shape and sharp edges. Specifically, the sharp edges of the graphitic sheets protrude at the top or edge of the point emitter, which yields an outstanding field emission performance.

The C-cork fiber-based point emitters have a low turn-on field of 0.7 V μm^{-1} as well as a high maximum current density of 45 $mA cm^{-2}$, as shown in Figure 5-13(b-c). Since the electric field is focused at the tip of the fiber in point emitters, a stronger electric field enhancement is observed, compared to the line emitters.

The Fowler-Nordheim (F-N) equation is useful for the analysis of field emission performance: [136-138]

$$J = a\varphi^{-1}\beta^2 E^2 \exp\left(-\frac{b\varphi^{\frac{3}{2}}}{\beta E}\right) \quad (1)$$

where J is the emission current density, φ is the work function of the graphite (5.0 eV), β is the field enhancement factor, and a and b are the Fowler-Nordheim constants, given as $1.56 \times 10^{-6}\, A \cdot V^{-2} \cdot eV, 6.83 \times 10^{7}\, V \cdot eV^{-\frac{3}{2}} \cdot cm^{-1}$, respectively. The field enhancement factor (β) indicates the

degree of electric field enhancement due to the field emitter's geometric effect:

$$\beta = -\frac{b\varphi^{3/2}}{m} \quad (2)$$

where φ is the work function of the graphite (5.0 eV), b is a constant ($6.83 \times 10^7\ V \cdot eV^{-\frac{3}{2}} \cdot cm^{-1}$), and m is the slope of the F-N curve. The inset of Figure 5-13(c) shows the F-N curve of the C-cork point emitter. The slope of the F-N curve (m=-6.2±0.1) yields the C-cork point emitter's field enhancement factor, which is 1.2×10^4, a remarkably high value resulting from the sharp edges of graphitic sheets and the fiber-type structure. This high enhancement factor ensures sufficient tunneling of electrons from the graphitic sheet surface through barriers, which results in a low turn-on electric field. Therefore, the emitter can provide a lower operating voltage and energy consumption, and a longer lifetime than commercial devices. The long-term stability of the C-cork point emitter was tested as shown in Figure 5-13(d). During the operation (approximately 12 h), the current density remained invariant at 10 and 30 $mAcm^{-2}$**.** The excellent stability of the emitter is attributed to the regular honeycomb surface morphology of the C-cork. Highly dense emission sites on the regular honeycomb surface with negligible screening effects assure a long-term stability without degradation of current density.

We compared the field emission performance of nanocarbon field emitters fabricated by various methods, such as graphene/rGO with EPD, spin coating, screen printing, and direct growth, and CNT with transfer method, direct growth, and others (Figure 5-13(e)).[11-24, 139-149] A striking feature of the performance is that the maximum current density is high and yet the turn-on voltage is very low. The high aspect ratio of the graphitic sheets and the absence of screening effect were responsible for the low turn-on voltage. Excellent electrical property of graphitic sheets and absence of contact resistance due to continuous structure of the sheets led to the high maximum current.

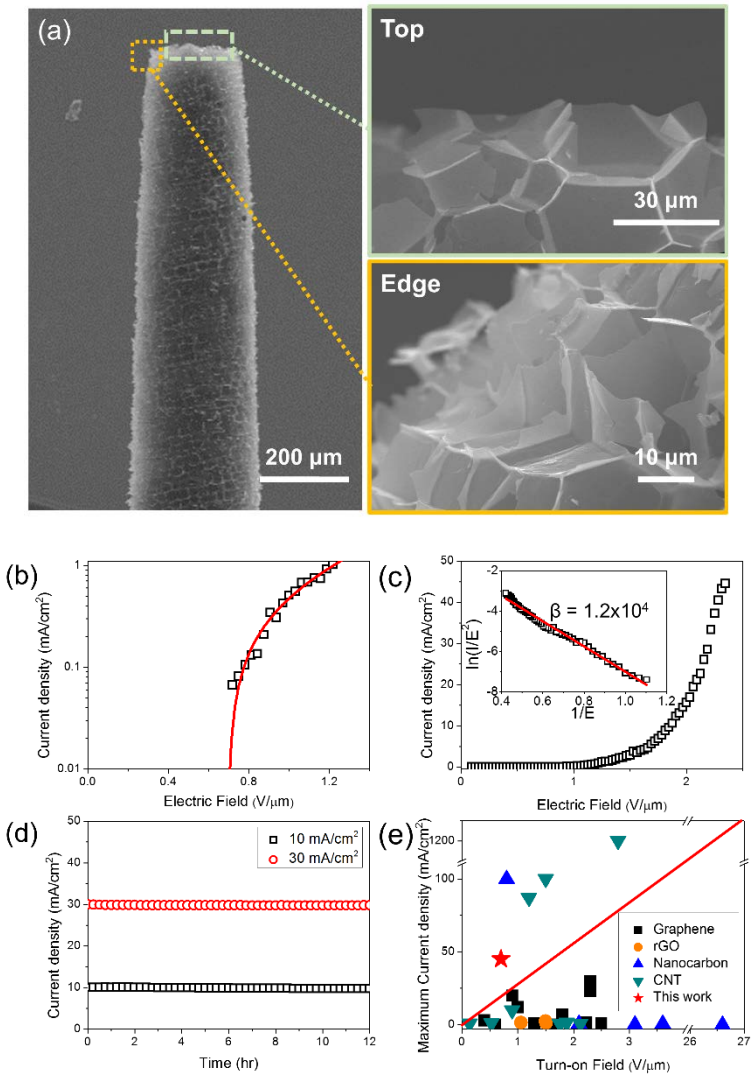

Figure 5-13. SEM images and field emission performance of point emitter of C-cork fiber. (a) SEM images of C-cork fiber from the tip and edge side. Field emission performances of C-cork point emitter at the region of (b) low and (c) entire electric field and the F-N curve of the C-cork point emitter. (d) Long-term stability of the C-cork point emitter with a current density of 10 and 30 $mAcm^{-2}$ for 12 h. (e) Comparison of turn-on field and maximum current

density that have been reported in the literature for nanocarbon field emitters.[11-24, 139-149]

5.4 Conclusion

In summary, we have demonstrated that the natural cork-based electron beam generator in the form of carbonized cork consumes a power much lower than the nanocarbon based generators for the same level of emitter performance. The cork emitter produces a high current density and long-term stability at the lowest turn-on field reported to date for nanocarbon emitters. The natural cork becomes graphitic honeycomb upon carbonization, with the cell walls 100-200 nm thick and the aspect ratio larger than 100, providing an ideal structure for the field emission. The nature of cork material makes it quite simple to fabricate the emitter. Furthermore, any desired shape of emitter tailored for the final application can easily be prepared. The fabrication of the cork emitter is not only facile and inexpensive but also eco-friendly. Other processes require a harmful chemical reaction, complicated manufacturing process, and cumbersome orientation process of nano carbon materials. Although the cork may not be scalable because of its ‘biological’ structure, the emitters made from the cork can be arrayed for large scale applications. With the features of lightness in weight and miniaturization capability comparable to commercial devices, the cork emitter introduced here would broaden the range of electron beam applications and bring the emitter closer to our daily lives.

Chapter 6. Conclusions

In this thesis, four novel approaches were developed in terms of fabricating the multidimensional field emitters. With the features of high current density and low turn-on field comparable to commercial devices, the nanocarbon field emitter introduced here would broaden the range of electron beam applications and bring the emitter closer to our daily lives.

1) CNT point emitter with graphene interfacial layer: In the present study the adoption of graphene as an interfacial layer between metal and CNT has been investigated. High quality graphene was uniformly grown on a copper wire. The interfacial graphene layer results in dramatic decrease of electrical contact resistance by an order of 2, and the increase of the interfacial thermal conductivity by 16%. Such a high improvement in electrical and thermal interface leads to the superior field emission performance with a very low turn-on field and a threshold field, as well as the maximum current. The emitter also shows stable emission characteristics with a high current for 10 hours.

2) CNT line emitter using clamping process: By applying mechanical compression with a controlled clamping margin to a vertically aligned CNT forest, a hemicylindrical shape of CNT structure strongly held with the tongs electrode was achieved. With the robust mechanical, thermal, and electrical

contacts created by the mechanical clamping process, the CNT line emitter, especially the bread-shaped emitter, showed superb field emission performance and stable operation of over 10 hours. We also fabricated the CNT multi-emitter composed of five bread-shaped emitters. Excellent field emission performances, including an extremely high current of 103 mA and emission stability for 10 hours, were achieved, showing the significant applicability of the present emitter for high-power electron beam sources

3) Holey graphene film as a planar field emitter: In summary, a new class of planar emitter has been introduced that outperforms by far the conventional planar emitter. An array of holes etched through a graphene film constitutes the holey planar emitter. In this emitter, the applied electric field is concentrated on the edge along the circumference of each hole and the edge of graphene film provides efficient field emission sites with a great amplification of field enhancement. The optimal hole size and the number of holes for a given film area can be obtained with the aid of Fowler-Nordheim equation. Unlike the conventional planar emitter, there is no dependence of the screening effect on the distance between emitters and neither is there a need for leveling the height of emitters because of the nature of the holey graphene film.

4) Carbonized cork emitter for multi-dimensional field emission: In summary, we have demonstrated that the natural cork-based electron beam generator in

the form of carbonized cork consumes a power much lower than the nanocarbon based generators for the same level of emitter performance. The cork emitter produces a high current density and long-term stability at the lowest turn-on field reported to date for nanocarbon emitters. The natural cork becomes graphitic honeycomb upon carbonization, with the cell walls 100-200 nm thick and the aspect ratio larger than 100, providing an ideal structure for the field emission. The nature of cork material makes it quite simple to fabricate the emitter. Furthermore, any desired shape of emitter tailored for the final application can easily be prepared. The fabrication of the cork emitter is not only facile and inexpensive but also eco-friendly. Other processes require a harmful chemical reaction, complicated manufacturing process, and cumbersome orientation process of nano carbon materials. Although the cork may not be scalable because of its 'biological' structure, the emitters made from the cork can be arrayed for large scale applications.

Bibliography

(1) Yue, G. Z.; Qiu, Q.; Gao, B.; Cheng, Y.; Zhang, J.; Shimoda, H.; Chang, S.; Lu, J. P.; Zhou, O. Generation of continuous and pulsed diagnostic imaging x-ray radiation using a carbon-nanotube-based field-emission cathode. *Appl. Phys. Lett.* **2002,** *81*, 355-357.

(2) Xiomara, C.-C.; Huaizhi, G.; Bo, G.; Lei, A.; Guohua, C.; Otto, Z. A carbon nanotube field emission cathode with high current density and long-term stability. *Nanotechnology* **2009,** *20*, 325707.

(3) Booske, J. H.; Dobbs, R. J.; Joye, C. D.; Kory, C. L.; Neil, G. R.; Park, G. S.; Park, J.; Temkin, R. J. Vacuum Electronic High Power Terahertz Sources. *IEEE Trans. Terahertz Sci. Technol.* **2011,** *1*, 54-75.

(4) Teo, K. B. K.; Minoux, E.; Hudanski, L.; Peauger, F.; Schnell, J.-P.; Gangloff, L.; Legagneux, P.; Dieumegard, D.; Amaratunga, G. A. J.; Milne, W. I. Microwave devices: Carbon nanotubes as cold cathodes. *Nature* **2005,** *437*, 968-968.

(5) Milne, W. I.; Teo, K. B. K.; Amaratunga, G. A. J.; Legagneux, P.; Gangloff, L.; Schnell, J. P.; Semet, V.; Thien Binh, V.; Groening, O. Carbon nanotubes as field emission sources. *J. Mater. Chem.* **2004,** *14*, 933-943.

(6) Jeong Seok, L.; Taewoo, K.; Seul-Gi, K.; Myung Rae, C.; Dong Kyun, S.; Minwoo, L.; Seontae, K.; Dae Weon, K.; Gun-Sik, P.; Dae Hong, J.; Yun

Daniel, P.; Ji-Beom, Y.; Tae June, K.; Yong Hyup, K. High performance CNT point emitter with graphene interfacial layer. *Nanotechnology* **2014,** *25*, 455601.

(7) Gao, B.; Yue, G. Z.; Qiu, Q.; Cheng, Y.; Shimoda, H.; Fleming, L.; Zhou, O. Fabrication and Electron Field Emission Properties of Carbon Nanotube Films by Electrophoretic Deposition. *Adv. Mater.* **2001,** *13*, 1770-1773.

(8) Jiang, K.; Wang, J.; Li, Q.; Liu, L.; Liu, C.; Fan, S. Superaligned Carbon Nanotube Arrays, Films, and Yarns: A Road to Applications. *Adv. Mater.* **2011,** *23*, 1154-1161.

(9) Yamaguchi, H.; Murakami, K.; Eda, G.; Fujita, T.; Guan, P.; Wang, W.; Gong, C.; Boisse, J.; Miller, S.; Acik, M.; Cho, K.; Chabal, Y. J.; Chen, M.; Wakaya, F.; Takai, M.; Chhowalla, M. Field Emission from Atomically Thin Edges of Reduced Graphene Oxide. *ACS Nano* **2011,** *5*, 4945-4952.

(10) Xiao, Z.; She, J.; Deng, S.; Tang, Z.; Li, Z.; Lu, J.; Xu, N. Field Electron Emission Characteristics and Physical Mechanism of Individual Single-Layer Graphene. *ACS Nano* **2010,** *4*, 6332-6336.

(11) Wu, Z.-S.; Pei, S.; Ren, W.; Tang, D.; Gao, L.; Liu, B.; Li, F.; Liu, C.; Cheng, H.-M. Field Emission of Single-Layer Graphene Films Prepared by Electrophoretic Deposition. *Adv. Mater.* **2009,** *21*, 1756-1760.

(12) Palnitkar, U. A.; Kashid, R. V.; More, M. A.; Joag, D. S.; Panchakarla, L. S.; Rao, C. N. R. Remarkably low turn-on field emission in undoped, nitrogen-doped, and boron-doped graphene. *Appl. Phys. Lett.* **2010,** *97*, 063102.

(13) Liu, J.; Zeng, B.; Wu, Z.; Sun, H. Enhanced Field Electron Emission of Graphene Sheets by CsI Coating after Electrophoretic Deposition. *ACS Appl. Mater. Interfaces* **2012,** *4*, 1219-1224.

(14) Maiti, U. N.; Maiti, S.; Das, N. S.; Chattopadhyay, K. K. Hierarchical graphene nanocones over 3D platform of carbon fabrics: A route towards fully foldable graphene based electron source. *Nanoscale* **2011,** *3*, 4135-4141.

(15) Stratakis, E.; Eda, G.; Yamaguchi, H.; Kymakis, E.; Fotakis, C.; Chhowalla, M. Free-standing graphene on microstructured silicon vertices for enhanced field emission properties. *Nanoscale* **2012,** *4*, 3069-3074.

(16) Hallam, T.; Cole, M. T.; Milne, W. I.; Duesberg, G. S. Field Emission Characteristics of Contact Printed Graphene Fins. *Small* **2014,** *10*, 95-99.

(17) Malesevic, A.; Kemps, R.; Vanhulsel, A.; Chowdhury, M. P.; Volodin, A.; Haesendonck, C. V. Field emission from vertically aligned few-layer graphene. *J. Appl. Phys.* **2008,** *104*, 084301.

(18) Qi, J. L.; Wang, X.; Zheng, W. T.; Tian, H. W.; Hu, C. Q.; Peng, Y. S. Ar plasma treatment on few layer graphene sheets for enhancing their field emission properties. *J. Phys. D: Appl. Phys.* **2010,** *43*, 055302.

(19) Jiang, L.; Yang, T.; Liu, F.; Dong, J.; Yao, Z.; Shen, C.; Deng, S.; Xu, N.; Liu, Y.; Gao, H.-J. Controlled Synthesis of Large-Scale, Uniform, Vertically Standing Graphene for High-Performance Field Emitters. *Adv. Mater.* **2013,** *25*, 250-255.

(20) Deng, J.-h.; Zheng, R.-t.; Zhao, Y.; Cheng, G.-a. Vapor–Solid Growth of Few-Layer Graphene Using Radio Frequency Sputtering Deposition and Its Application on Field Emission. *ACS Nano* **2012,** *6*, 3727-3733.

(21) Yu, Z.; Jiale, D.; Shuai, T.; Pei, L.; Shaozhi, D.; Jun, C.; Ningsheng, X. Optimize the field emission character of a vertical few-layer graphene sheet by manipulating the morphology. *Nanotechnology* **2012,** *23*, 015202.

(22) Min, Q.; Tao, F.; Hui, D.; Lifeng, L.; Haibo, L.; Yiwei, C.; Zhuo, S. Electron field emission from screen-printed graphene films. *Nanotechnology* **2009,** *20*, 425702.

(23) Kim, T.; Lee, J. S.; Li, K.; Kang, T. J.; Kim, Y. H. High performance graphene foam emitter. *Carbon* **2016,** *101*, 345-351.

(24) Jeong, H. J.; Jeong, H. D.; Kim, H. Y.; Kim, S. H.; Kim, J. S.; Jeong, S. Y.; Han, J. T.; Lee, G.-W. Flexible Field Emission from Thermally Welded Chemically Doped Graphene Thin Films. *Small* **2012,** *8*, 272-280.

(25) Wei, W.; Liu, Y.; Wei, Y.; Jiang, K.; Peng, L.-M.; Fan, S. Tip Cooling Effect and Failure Mechanism of Field-Emitting Carbon Nanotubes. *Nano Lett.* **2006,** *7*, 64-68.

(26) Huang, J. Y.; Chen, S.; Jo, S. H.; Wang, Z.; Han, D. X.; Chen, G.; Dresselhaus, M. S.; Ren, Z. F. Atomic-Scale Imaging of Wall-by-Wall Breakdown and Concurrent Transport Measurements in Multiwall Carbon Nanotubes. *Phys. Rev. Lett.* **2005,** *94*, 236802.

(27) Smith, R. C.; Carey, J. D.; Cox, D. C.; Silva, S. R. P. In situ electrode manipulation for three terminal field emission characterization of individual carbon nanotubes. *Appl. Phys. Lett.* **2006,** *89*, 063111.

(28) Liu, J.; She, J.; Deng, S.; Chen, J.; Xu, N. Ultrathin Seed-Layer for Tuning Density of ZnO Nanowire Arrays and Their Field Emission Characteristics. *J. Phys. Chem. C* **2008,** *112*, 11685-11690.

(29) Bonard, J. M.; Weiss, N.; Kind, H.; Stöckli, T.; Forró, L.; Kern, K.; Châtelain, A. Tuning the Field Emission Properties of Patterned Carbon Nanotube Films. *Advanced Materials* **2001,** *13*, 184-188.

(30) Baughman, R. H.; Zakhidov, A. A.; de Heer, W. A. Carbon Nanotubes--the Route Toward Applications. *Science* **2002,** *297*, 787-792.

(31) Minoux, E.; Groening, O.; Teo, K. B. K.; Dalal, S. H.; Gangloff, L.; Schnell, J.-P.; Hudanski, L.; Bu, I. Y. Y.; Vincent, P.; Legagneux, P.; Amaratunga, G. A. J.; Milne, W. I. Achieving High-Current Carbon Nanotube Emitters. *Nano letters* **2005,** *5*, 2135-2138.

(32) Zhu, L.; Sun, Y.; Hess, D. W.; Wong, C.-P. Well-Aligned Open-Ended Carbon Nanotube Architectures: An Approach for Device Assembly. *Nano letters* **2006,** *6*, 243-247.

(33) Perea-López, N.; Rebollo-Plata, B.; Briones-León, J. A.; Morelos-Gómez, A.; Hernández-Cruz, D.; Hirata, G. A.; Meunier, V.; Botello-Méndez, A. R.; Charlier, J.-C.; Maruyama, B.; Muñoz-Sandoval, E.; López-Urías, F.; Terrones, M.; Terrones, H. Millimeter-Long Carbon Nanotubes: Outstanding Electron-Emitting Sources. *ACS Nano* **2011,** *5*, 5072-5077.

(34) Liu, P.; Wei, Y.; Liu, K.; Liu, L.; Jiang, K.; Fan, S. New-Type Planar Field Emission Display with Superaligned Carbon Nanotube Yarn Emitter. *Nano letters* **2012,** *12*, 2391-2396.

(35) Yuge, R.; Miyawaki, J.; Ichihashi, T.; Kuroshima, S.; Yoshitake, T.; Ohkawa, T.; Aoki, Y.; Iijima, S.; Yudasaka, M. Highly Efficient Field Emission from Carbon Nanotube−Nanohorn Hybrids Prepared by Chemical Vapor Deposition. *ACS Nano* **2010,** *4*, 7337-7343.

(36) Sugie, H.; Tanemura, M.; Filip, V.; Iwata, K.; Takahashi, K.; Okuyama, F. Carbon nanotubes as electron source in an x-ray tube. *Applied Physics Letters* **2001,** *78*, 2578-2580.

(37) Ferrer, D.; Tanii, T.; Matsuya, I.; Zhong, G.; Okamoto, S.; Kawarada, H.; Shinada, T.; Ohdomari, I. Enhancement of field emission characteristics

of tungsten emitters by single-walled carbon nanotube modification. *Applied Physics Letters* **2006,** *88*, -.

(38) Chen, G.; Shin, D. H.; Roth, S.; Lee, C. J. Field emission characteristics of point emitters fabricated by a multiwalled carbon nanotube yarn. *Nanotechnology* **2009,** *20*, 315201.

(39) Zhang, S.; Koziol, K. K. K.; Kinloch, I. A.; Windle, A. H. Macroscopic Fibers of Well-Aligned Carbon Nanotubes by Wet Spinning. *Small* **2008,** *4*, 1217-1222.

(40) Kim, W. J.; Jang, E. Y.; Seo, D. K.; Kang, T. J.; Jin, K. C.; Jeong, D. H.; Kim, Y. H. Crystal-like Growth of a Metal Oxide/CNT Composite Fiber with Electroplated “Seed” from a CNT-Dispersed Nonaqueous Electrolyte. *Langmuir : the ACS journal of surfaces and colloids* **2010,** *26*, 15701-15705.

(41) Jung, S. I.; Choi, J. S.; Shim, H. C.; Kim, S.; Jo, S. H.; Lee, C. J. Fabrication of probe-typed carbon nanotube point emitters. *Applied Physics Letters* **2006,** *89*, -.

(42) Liu, N.; Fang, G.; Zeng, W.; Zhou, H.; Long, H.; Zhao, X. Enhanced field emission from three-dimensional patterned carbon nanotube arrays grown on flexible carbon cloth. *Journal of Materials Chemistry* **2012,** *22*, 3478-3484.

(43) Das, S.; Seelaboyina, R.; Verma, V.; Lahiri, I.; Hwang, J. Y.; Banerjee, R.; Choi, W. Synthesis and characterization of self-organized multilayered

graphene-carbon nanotube hybrid films. *Journal of Materials Chemistry* **2011,** *21*, 7289-7295.

(44) Wu, C.; Li, F.; Zhang, Y.; Guo, T. Improving the field emission of graphene by depositing zinc oxide nanorods on its surface. *Carbon* **2012,** *50*, 3622-3626.

(45) Neupane, S.; Lastres, M.; Chiarella, M.; Li, W.; Su, Q.; Du, G. Synthesis and field emission properties of vertically aligned carbon nanotube arrays on copper. *Carbon* **2012,** *50*, 2641-2650.

(46) Chen, C.; Liu, L.; Lu, Y.; Kong, E. S.-W.; Zhang, Y.; Sheng, X.; Ding, H. A method for creating reliable and low-resistance contacts between carbon nanotubes and microelectrodes. *Carbon* **2007,** *45*, 436-442.

(47) Rykaczewski, K.; Henry, M. R.; Kim, S.-K.; Fedorov, A. G.; Kulkarni, D.; Singamaneni, S.; Tsukruk, V. V. The effect of the geometry and material properties of a carbon joint produced by electron beam induced deposition on the electrical resistance of a multiwalled carbon nanotube-to-metal contact interface. *Nanotechnology* **2010,** *21*, 035202.

(48) Kane, A. A.; Sheps, T.; Branigan, E. T.; Apkarian, V. A.; Cheng, M. H.; Hemminger, J. C.; Hunt, S. R.; Collins, P. G. Graphitic Electrical Contacts to Metallic Single-Walled Carbon Nanotubes Using Pt Electrodes. *Nano letters* **2009,** *9*, 3586-3591.

(49) Javey, A.; Guo, J.; Wang, Q.; Lundstrom, M.; Dai, H. Ballistic carbon nanotube field-effect transistors. *Nature* **2003,** *424,* 654-657.

(50) Woo, Y.; Duesberg, G. S.; Roth, S. Reduced contact resistance between an individual single-walled carbon nanotube and a metal electrode by a local point annealing. *Nanotechnology* **2007,** *18,* 095203.

(51) Biswas, C.; Lee, Y. H. Graphene Versus Carbon Nanotubes in Electronic Devices. *Advanced Functional Materials* **2011,** *21,* 3806-3826.

(52) Saito, Y.; Iizuka, T.; Koretsune, T.; Arita, R.; Shimizu, S.; Iwasa, Y. Gate-Tuned Thermoelectric Power in Black Phosphorus. *Nano Lett.* **2016**.

(53) Giovannetti, G.; Khomyakov, P. A.; Brocks, G.; Karpan, V. M.; van den Brink, J.; Kelly, P. J. Doping Graphene with Metal Contacts. *Physical Review Letters* **2008,** *101,* 026803.

(54) Pei, T.; Xu, H.; Zhang, Z.; Wang, Z.; Liu, Y.; Li, Y.; Wang, S.; Peng, L.-M. Electronic transport in single-walled carbon nanotube/graphene junction. *Applied Physics Letters* **2011,** *99,* -.

(55) Kim, W. J.; Lee, J. S.; Lee, S. M.; Song, K. Y.; Chu, C. N.; Kim, Y. H. Better than 10 mA Field Emission from an Isolated Structure Emitter of a Metal Oxide/CNT Composite. *ACS Nano* **2010,** *5,* 429-435.

(56) Kerfriden, S.; Nahlé, A. H.; Campbell, S. A.; Walsh, F. C.; Smith, J. R. Short CommunicationThe electrochemical etching of tungsten STM tips. *Electrochimica Acta* **1998,** *43,* 1939-1944.

(57) Chung, M. G.; Kim, D. H.; Lee, H. M.; Kim, T.; Choi, J. H.; Seo, D. k.; Yoo, J.-B.; Hong, S.-H.; Kang, T. J.; Kim, Y. H. Highly sensitive NO2 gas sensor based on ozone treated graphene. *Sensors and Actuators B: Chemical* **2012,** *166–167*, 172-176.

(58) Lee, S.; Lee, K.; Zhong, Z. Wafer Scale Homogeneous Bilayer Graphene Films by Chemical Vapor Deposition. *Nano letters* **2010,** *10*, 4702-4707.

(59) Lim, S. C.; Jang, J. H.; Bae, D. J.; Han, G. H.; Lee, S.; Yeo, I.-S.; Lee, Y. H. Contact resistance between metal and carbon nanotube interconnects: Effect of work function and wettability. *Applied Physics Letters* **2009,** *95*, -.

(60) Lee, S.; Kahng, S. J.; Kuk, Y. Nano-level wettings of platinum and palladium on single-walled carbon nanotubes. *Chemical Physics Letters* **2010,** *500*, 82-85.

(61) Zhang, Y.; Franklin, N. W.; Chen, R. J.; Dai, H. Metal coating on suspended carbon nanotubes and its implication to metal–tube interaction. *Chemical Physics Letters* **2000,** *331*, 35-41.

(62) Yang, C.; Hazeghi, A.; Takei, K.; Hong-Yu, C.; Chan, P. C. H.; Javey, A.; Wong, H. S. P. Low-Resistance Electrical Contact to Carbon Nanotubes With Graphitic Interfacial Layer. *Electron Devices, IEEE Transactions on* **2012,** *59*, 12-19.

(63) Yen, M.-Y.; Hsiao, M.-C.; Liao, S.-H.; Liu, P.-I.; Tsai, H.-M.; Ma, C.-C. M.; Pu, N.-W.; Ger, M.-D. Preparation of graphene/multi-walled carbon nanotube hybrid and its use as photoanodes of dye-sensitized solar cells. *Carbon* **2011,** *49,* 3597-3606.

(64) Huang, J.-H.; Fang, J.-H.; Liu, C.-C.; Chu, C.-W. Effective Work Function Modulation of Graphene/Carbon Nanotube Composite Films As Transparent Cathodes for Organic Optoelectronics. *ACS Nano* **2011,** *5,* 6262-6271.

(65) Liang, X.; Sperling, B. A.; Calizo, I.; Cheng, G.; Hacker, C. A.; Zhang, Q.; Obeng, Y.; Yan, K.; Peng, H.; Li, Q.; Zhu, X.; Yuan, H.; Hight Walker, A. R.; Liu, Z.; Peng, L.-m.; Richter, C. A. Toward Clean and Crackless Transfer of Graphene. *ACS Nano* **2011,** *5,* 9144-9153.

(66) Li, X.; Zhu, Y.; Cai, W.; Borysiak, M.; Han, B.; Chen, D.; Piner, R. D.; Colombo, L.; Ruoff, R. S. Transfer of Large-Area Graphene Films for High-Performance Transparent Conductive Electrodes. *Nano letters* **2009,** *9,* 4359-4363.

(67) Sveningsson, M.; Hansen, K.; Svensson, K.; Olsson, E.; Campbell, E. E. B. Quantifying temperature-enhanced electron field emission from individual carbon nanotubes. *Physical Review B* **2005,** *72,* 085429.

(68) Purcell, S. T.; Vincent, P.; Journet, C.; Binh, V. T. Hot Nanotubes: Stable Heating of Individual Multiwall Carbon Nanotubes to 2000 K Induced by the Field-Emission Current. *Physical Review Letters* **2002,** *88*, 105502.

(69) Pan, J. Y.; Zhu, C. C.; Gao, Y. L. Enhanced field emission characteristics of zinc oxide mixed carbon nano-tubes films. *Applied Surface Science* **2008,** *254*, 3787-3792.

(70) de Jonge, N.; Lamy, Y.; Schoots, K.; Oosterkamp, T. H. High brightness electron beam from a multi-walled carbon nanotube. *Nature* **2002,** *420*, 393-395.

(71) de Heer, W. A.; Châtelain, A.; Ugarte, D. A Carbon Nanotube Field-Emission Electron Source. *Science* **1995,** *270*, 1179-1180.

(72) de Heer, W. A.; Bonard, J.-M.; Fauth, K.; Châtelain, A.; Ugarte, D.; Forró, L. Electron field emitters based on carbon nanotube films. *Adv. Mater.* **1997,** *9*, 87-89.

(73) Wang, B. B.; Cheng, Q. J.; Chen, X.; Ostrikov, K. Enhancement of electron field emission of vertically aligned carbon nanotubes by nitrogen plasma treatment. *Journal of Alloys and Compounds* **2011,** *509*, 9329-9334.

(74) Chen, L.; He, H.; Yu, H.; Cao, Y.; Lei, D.; Menggen, Q.; Wu, C.; Hu, L. Electron field emission characteristics of graphene/carbon nanotubes hybrid field emitter. *Journal of Alloys and Compounds* **2014,** *610*, 659-664.

(75) deHeer, W. A.; Bacsa, W. S.; Châtelain, A.; Gerfin, T.; Humphrey-Baker, R.; Forro, L.; Ugarte, D. Aligned Carbon Nanotube Films: Production and Optical and Electronic Properties. *Science* **1995,** *268,* 845-847.

(76) Abbas, S. M.; Ali, S.; Niaz, N. A.; Ali, N.; Ahmed, R.; Ahmad, N. Superior electrochemical performance of mesoporous Fe3O4/CNT nanocomposites as anode material for lithium ion batteries. *Journal of Alloys and Compounds* **2014,** *611*, 260-266.

(77) Phuong, D. D.; Trinh, P. V.; An, N. V.; Luan, N. V.; Minh, P. N.; Khisamov, R. K.; Nazarov, K. S.; Zubairov, L. R.; Mulyukov, R. R.; Nazarov, A. A. Effects of carbon nanotube content and annealing temperature on the hardness of CNT reinforced aluminum nanocomposites processed by the high pressure torsion technique. *Journal of Alloys and Compounds* **2014,** *613,* 68-73.

(78) Collins, P. G.; Zettl, A. A simple and robust electron beam source from carbon nanotubes. *Applied Physics Letters* **1996,** *69,* 1969-1971.

(79) Kibis, O. V.; Portnoi, M. E. Carbon nanotubes: A new type of emitter in the terahertz range. *Tech. Phys. Lett.* **2005,** *31,* 671-672.

(80) Ci, L.; Punbusayakul, N.; Wei, J.; Vajtai, R.; Talapatra, S.; Ajayan, P. M. Multifunctional Macroarchitectures of Double-Walled Carbon Nanotube Fibers. *Advanced Materials* **2007,** *19,* 1719-1723.

(81) Guohai, C.; Dong Hoon, S.; Siegmar, R.; Cheol Jin, L. Field emission characteristics of point emitters fabricated by a multiwalled carbon nanotube yarn. *Nanotechnology* **2009,** *20*, 315201.

(82) Kuznetzov, A. A.; Lee, S. B.; Zhang, M.; Baughman, R. H.; Zakhidov, A. A. Electron field emission from transparent multiwalled carbon nanotube sheets for inverted field emission displays. *Carbon* **2010,** *48*, 41-46.

(83) Jang, E. Y.; Kang, T. J.; Im, H.; Baek, S. J.; Kim, S.; Jeong, D. H.; Park, Y. W.; Kim, Y. H. Macroscopic Single-Walled-Carbon-Nanotube Fiber Self-Assembled by Dip-Coating Method. *Advanced Materials* **2009,** *21*, 4357-4361.

(84) Correa-Duarte, M. A.; Wagner, N.; Rojas-Chapana, J.; Morsczeck, C.; Thie, M.; Giersig, M. Fabrication and Biocompatibility of Carbon Nanotube-Based 3D Networks as Scaffolds for Cell Seeding and Growth. *Nano Letters* **2004,** *4*, 2233-2236.

(85) Jang, E. Y.; Kang, T. J.; Im, H. W.; Kim, D. W.; Kim, Y. H. Single-Walled Carbon-Nanotube Networks on Large-Area Glass Substrate by the Dip-Coating Method. *Small* **2008,** *4*, 2255-2261.

(86) Zhang, M.; Fang, S.; Zakhidov, A. A.; Lee, S. B.; Aliev, A. E.; Williams, C. D.; Atkinson, K. R.; Baughman, R. H. Strong, Transparent, Multifunctional, Carbon Nanotube Sheets. *Science* **2005,** *309*, 1215-1219.

(87) Li, Q. W.; Li, Y.; Zhang, X. F.; Chikkannanavar, S. B.; Zhao, Y. H.; Dangelewicz, A. M.; Zheng, L. X.; Doorn, S. K.; Jia, Q. X.; Peterson, D. E.; Arendt, P. N.; Zhu, Y. T. Structure-Dependent Electrical Properties of Carbon Nanotube Fibers. *Advanced Materials* **2007,** *19*, 3358-3363.

(88) Vigolo, B.; Pénicaud, A.; Coulon, C.; Sauder, C.; Pailler, R.; Journet, C.; Bernier, P.; Poulin, P. Macroscopic Fibers and Ribbons of Oriented Carbon Nanotubes. *Science* **2000,** *290*, 1331-1334.

(89) Wu, Z.; Chen, Z.; Du, X.; Logan, J. M.; Sippel, J.; Nikolou, M.; Kamaras, K.; Reynolds, J. R.; Tanner, D. B.; Hebard, A. F.; Rinzler, A. G. Transparent, Conductive Carbon Nanotube Films. *Science* **2004,** *305*, 1273-1276.

(90) Aliev, A. E.; Guthy, C.; Zhang, M.; Fang, S.; Zakhidov, A. A.; Fischer, J. E.; Baughman, R. H. Thermal transport in MWCNT sheets and yarns. *Carbon* **2007,** *45*, 2880-2888.

(91) Patole, S. P.; Alegaonkar, P. S.; Lee, H.-C.; Yoo, J.-B. Optimization of water assisted chemical vapor deposition parameters for super growth of carbon nanotubes. *Carbon* **2008,** *46*, 1987-1993.

(92) Liu, C.; Tong, Y.; Cheng, H.-M.; Golberg, D.; Bando, Y. Field emission properties of macroscopic single-walled carbon nanotube strands. *Applied Physics Letters* **2005,** *86*, 223114-3.

(93) Nilsson, L.; Groening, O.; Emmenegger, C.; Kuettel, O.; Schaller, E.; Schlapbach, L.; Kind, H.; Bonard, J. M.; Kern, K. Scanning field emission from patterned carbon nanotube films. *Applied Physics Letters* **2000,** *76*, 2071-2073.

(94) Yeh, C. M.; Chen, M. Y.; Hwang, J.; Gan, J. Y.; Kou, C. S. Field emission from a composite structure consisting of vertically aligned single-walled carbon nanotubes and carbon nanocones. *Nanotechnology* **2006,** *17*, 5930.

(95) Bonard, J.-M.; Salvetat, J.-P.; Stockli, T.; de Heer, W. A.; Forro, L.; Chatelain, A. Field emission from single-wall carbon nanotube films. *Applied Physics Letters* **1998,** *73*, 918-920.

(96) Wei, Y.; Jiang; Liu, L.; Chen, Z.; Fan Vacuum-Breakdown-Induced Needle-Shaped Ends of Multiwalled Carbon Nanotube Yarns and Their Field Emission Applications. *Nano Letters* **2007,** *7*, 3792-3797.

(97) Xu, J.; Pan, R.; Chen, Y.; Piao, X.; Qian, M.; Feng, T.; Sun, Z. Electron field emission from screen-printed graphene/DWCNT composite films. *Journal of Alloys and Compounds* **2013,** *551*, 348-351.

(98) Choi, J. S.; Lee, H. S.; Goak, J. C.; Seo, Y.; Kim, K. B.; Song, Y. H.; Choi, Y. C.; Lee, N. S. Field emission characteristics of carbon nanotube films fabricated on a metal mesh by filtration. *Journal of Alloys and Compounds* **2012,** *521*, 126-133.

(99) Ok, J. G.; Kim, B. H.; Sung, W. Y.; Chu, C. N.; Kim, Y. H. Uniformity enhancement of carbon nanofiber emitters via electrical discharge machining. *Applied Physics Letters* **2007,** *90*, 033117-3.

(100) Zhang, Y.; Liao, M. X.; Deng, S. Z.; Chen, J.; Xu, N. S. In situ oxygen-assisted field emission treatment for improving the uniformity of carbon nanotube pixel arrays and the underlying mechanism. *Carbon* **2011,** *49*, 3299-3306.

(101) Singh, V.; Joung, D.; Zhai, L.; Das, S.; Khondaker, S. I.; Seal, S. Graphene based materials: Past, present and future. *Progress in Materials Science* **2011,** *56*, 1178-1271.

(102) Dean, K. A.; Burgin, T. P.; Chalamala, B. R. Evaporation of carbon nanotubes during electron field emission. *Applied Physics Letters* **2001,** *79*, 1873-1875.

(103) She, J. C.; Xu, N. S.; Deng, S. Z.; Chen, J.; Bishop, H.; Huq, S. E.; Wang, L.; Zhong, D. Y.; Wang, E. G. Vacuum breakdown of carbon-nanotube field emitters on a silicon tip. *Applied Physics Letters* **2003,** *83*, 2671-2673.

(104) Suh, J. S.; Jeong, K. S.; Lee, J. S.; Han, I. Study of the field-screening effect of highly ordered carbon nanotube arrays. *Applied Physics Letters* **2002,** *80*, 2392-2394.

(105) Nilsson, L.; Groening, O.; Emmenegger, C.; Kuettel, O.; Schaller, E.; Schlapbach, L.; Kind, H.; Bonard, J.-M.; Kern, K. Scanning field emission

from patterned carbon nanotube films. *Applied Physics Letters* **2000,** *76*, 2071-2073.

(106) Stankovich, S.; Dikin, D. A.; Piner, R. D.; Kohlhaas, K. A.; Kleinhammes, A.; Jia, Y.; Wu, Y.; Nguyen, S. T.; Ruoff, R. S. Synthesis of graphene-based nanosheets via chemical reduction of exfoliated graphite oxide. *Carbon* **2007,** *45*, 1558-1565.

(107) Mattevi, C.; Eda, G.; Agnoli, S.; Miller, S.; Mkhoyan, K. A.; Celik, O.; Mastrogiovanni, D.; Granozzi, G.; Garfunkel, E.; Chhowalla, M. Evolution of Electrical, Chemical, and Structural Properties of Transparent and Conducting Chemically Derived Graphene Thin Films. *Advanced Functional Materials* **2009,** *19*, 2577-2583.

(108) Seungwoo, J.; Ki-Bum, K.; Gustavo, F.; Jin Ho, K.; Fazal, W.; Jimmy, X. Enhanced thermoelectric power in nanopatterned carbon nanotube film. *Nanotechnology* **2012,** *23*, 135704.

(109) Cai, D.; Liu, L. The screening effects of carbon nanotube arrays and its field emission optimum density. *AIP Advances* **2013,** *3*, 122103.

(110) Smith, R. C.; Silva, S. R. P. Maximizing the electron field emission performance of carbon nanotube arrays. *Applied Physics Letters* **2009,** *94*, 133104.

(111) Ok, J. G.; Kim, B. H.; Sung, W. Y.; Chu, C. N.; Kim, Y. H. Uniformity enhancement of carbon nanofiber emitters via electrical discharge machining. *Applied Physics Letters* **2007,** *90*, 033117.

(112) Kim, Y. C.; Nam, J. W.; Hwang, M. I.; Kim, I. H.; Lee, C. S.; Choi, Y. C.; Park, J. H.; Kim, H. S.; Kim, J. M. Uniform and stable field emission from printed carbon nanotubes through oxygen trimming. *Applied Physics Letters* **2008,** *92*, 263112.

(113) Liang, X. H.; Deng, S. Z.; Xu, N. S.; Chen, J.; Huang, N. Y.; She, J. C. On achieving better uniform carbon nanotube field emission by electrical treatment and the underlying mechanism. *Applied Physics Letters* **2006,** *88*, 111501.

(114) Yan, X.; Tay, B.-K.; Miele, P. Field emission from ordered carbon nanotube-ZnO heterojunction arrays. *Carbon* **2008,** *46*, 753-758.

(115) Lahiri, I.; Verma, V. P.; Choi, W. An all-graphene based transparent and flexible field emission device. *Carbon* **2011,** *49*, 1614-1619.

(116) Hwang, J. O.; Lee, D. H.; Kim, J. Y.; Han, T. H.; Kim, B. H.; Park, M.; No, K.; Kim, S. O. Vertical ZnO nanowires/graphene hybrids for transparent and flexible field emission. *Journal of Materials Chemistry* **2011,** *21*, 3432-3437.

(117) Lee, D. H.; Lee, J. A.; Lee, W. J.; Kim, S. O. Flexible Field Emission of Nitrogen-Doped Carbon Nanotubes/Reduced Graphene Hybrid Films. *Small* **2011,** *7*, 95-100.

(118) Lee, D. H.; Lee, J. A.; Lee, W. J.; Choi, D. S.; Lee, W. J.; Kim, S. O. Facile Fabrication and Field Emission of Metal-Particle-Decorated Vertical N-Doped Carbon Nanotube/Graphene Hybrid Films. *The Journal of Physical Chemistry C* **2010,** *114*, 21184-21189.

(119) Hung, Y., Jr.; Huang, Y.-J.; Chang, H.-C.; Lee, K.-Y.; Lee, S.-L. Patterned growth of carbon nanotubes over vertically aligned silicon nanowire bundles for achieving uniform field emission. *Nanoscale Res Lett* **2014,** *9*, 1-7.

(120) Guohai, C.; Dong Hoon, S.; Suki, K.; Siegmar, R.; Cheol Jin, L. Improved field emission stability of thin multiwalled carbon nanotube emitters. *Nanotechnology* **2010,** *21*, 015704.

(121) Huang, B.-R.; Lin, T.-C.; Chu, J. P.; Chen, Y.-C. Long-term stability of a horizontally-aligned carbon nanotube field emission cathode coated with a metallic glass thin film. *Carbon* **2012,** *50*, 1619-1624.

(122) Deldicque, D.; Rouzaud, J.-N.; Velde, B. A Raman − HRTEM study of the carbonization of wood: A new Raman-based paleothermometer dedicated to archaeometry. *Carbon* **2016,** *102*, 319-329.

(123) Hu, H.; Zhao, Z.; Wan, W.; Gogotsi, Y.; Qiu, J. Ultralight and Highly Compressible Graphene Aerogels. *Adv. Mater.* **2013,** *25*, 2219-2223.

(124) Park, S.; Lee, K.-S.; Bozoklu, G.; Cai, W.; Nguyen, S. T.; Ruoff, R. S. Graphene Oxide Papers Modified by Divalent Ions—Enhancing Mechanical Properties via Chemical Cross-Linking. *ACS Nano* **2008,** *2*, 572-578.

(125) Zhang, J.; Yang, H.; Shen, G.; Cheng, P.; Zhang, J.; Guo, S. Reduction of graphene oxide vial-ascorbic acid. *Chem. Commun.* **2010,** *46*, 1112-1114.

(126) Gómez-Navarro, C.; Weitz, R. T.; Bittner, A. M.; Scolari, M.; Mews, A.; Burghard, M.; Kern, K. Electronic Transport Properties of Individual Chemically Reduced Graphene Oxide Sheets. *Nano Lett.* **2007,** *7*, 3499-3503.

(127) Chen, S.; Xin, Y.; Zhou, Y.; Zhang, F.; Ma, Y.; Zhou, H.; Qi, L. Branched CNT@SnO2 nanorods@carbon hierarchical heterostructures for lithium ion batteries with high reversibility and rate capability. *J. Mater. Chem. A* **2014,** *2*, 15582-15589.

(128) Viculis, L. M.; Mack, J. J.; Mayer, O. M.; Hahn, H. T.; Kaner, R. B. Intercalation and exfoliation routes to graphite nanoplatelets. *J. Mater. Chem.* **2005,** *15*, 974-978.

(129) Liu, W.-W.; Chai, S.-P.; Mohamed, A. R.; Hashim, U. Synthesis and characterization of graphene and carbon nanotubes: A review on the past and recent developments. *J. Ind. Eng. Chem.* **2014,** *20*, 1171-1185.

(130) Harutyunyan, A. R.; Pradhan, B. K.; Chang, J.; Chen, G.; Eklund, P. C. Purification of Single-Wall Carbon Nanotubes by Selective Microwave Heating of Catalyst Particles. *J. Phys. Chem. B* **2002,** *106*, 8671-8675.

(131) Kim, K. S.; Imris, M.; Shahverdi, A.; Alinejad, Y.; Soucy, G. Single-Walled Carbon Nanotubes Prepared by Large-Scale Induction Thermal Plasma Process: Synthesis, Characterization, and Purification. *J. Phys. Chem. C* **2009,** *113*, 4340-4348.

(132) Cao, J.; Xiao, G.; Xu, X.; Shen, D.; Jin, B. Study on carbonization of lignin by TG-FTIR and high-temperature carbonization reactor. *Fuel Process. Technol.* **2013,** *106*, 41-47.

(133) Deldicque, D.; Rouzaud, J.-N.; Velde, B. A Raman – HRTEM study of the carbonization of wood: A new Raman-based paleothermometer dedicated to archaeometry. *Carbon* **2016,** *102*, 319-329.

(134) Garlow, J. A.; Barrett, L. K.; Wu, L.; Kisslinger, K.; Zhu, Y.; Pulecio, J. F. Large-Area Growth of Turbostratic Graphene on Ni(111) via Physical Vapor Deposition. *Sci. Rep.* **2016,** *6*, 19804.

(135) Morgan, P., *Carbon Fibers and Their Composites*. Taylor & Francis: 2005.

(136) Forbes, R. G. Refining the application of Fowler–Nordheim theory. *Ultramicroscopy* **1999,** *79*, 11-23.

(137) Forbes, R. G. Physics of generalized Fowler-Nordheim-type equations. *J. Vac. Sci. Technol., B: Microelectron. Nanometer Struct.--Process., Meas., Phenom.* **2008,** *26*, 788-793.

(138) Hsu, C.-L.; Su, C.-W.; Hsueh, T.-J. Enhanced field emission of Al-doped ZnO nanowires grown on a flexible polyimide substrate with UV exposure. *RSC Adv.* **2014,** *4*, 2980-2983.

(139) Deng, J.-H.; Liu, R.-N.; Zhang, Y.; Zhu, W.-X.; Han, A. L.; Cheng, G.-A. Highly improved field emission from vertical graphene–carbon nanotube composites. *J. Alloys Compd.* **2017,** *723*, 75-83.

(140) Wang, Y.; Wei, Q.; Yu, Z.; Long, H.; Deng, Z.; Xie, Y.; Li, J.; Lin, C.-T.; Ma, L.; Zhou, K. Field emission properties of the caterpillar-like structural carbon film grown by magnetic and electric fields coupling HFCVD. *Appl. Surf. Sci.* **2017,** *423*, 788-792.

(141) Gay, S.; Orlanducci, S.; Passeri, D.; Rossi, M.; Terranova, M. L. Nanoshaping field emitters from glassy carbon sheets: a new functionality induced by H-plasma etching. *Phys. Chem. Chem. Phys.* **2016,** *18*, 25364-25372.

(142) Rakhi, R. B.; Sethupathi, K.; Ramaprabhu, S. Field emission from carbon nanotubes on a graphitized carbon fabric. *Carbon* **2008,** *46*, 1656-1663.

(143) Jeong, H. J.; Jeong, H. D.; Kim, H. Y.; Kim, J. S.; Jeong, S. Y.; Han, J. T.; Bang, D. S.; Lee, G.-W. All-Carbon Nanotube-Based Flexible Field-Emission Devices: From Cathode to Anode. *Adv. Funct. Mater.* **2011,** *21*, 1526-1532.

(144) Kim, K.; Lee, S. H.; Yi, W.; Kim, J.; Choi, J. W.; Park, Y.; Jin, J. I. Efficient Field Emission from Highly Aligned, Graphitic Nanotubes Embedded with Gold Nanoparticles. *Adv. Mater.* **2003,** *15*, 1618-1622.

(145) Kim, S. H.; Kim, D. U.; Lee, S. K. Elongation of vertically well-aligned carbon nanofiber bundles and their field emission characteristics. *Curr. Appl. Phys.* **2006,** *6*, 766-771.

(146) Sridhar, S.; Tiwary, C.; Vinod, S.; Taha-Tijerina, J. J.; Sridhar, S.; Kalaga, K.; Sirota, B.; Hart, A. H. C.; Ozden, S.; Sinha, R. K.; Harsh; Vajtai, R.; Choi, W.; Kordás, K.; Ajayan, P. M. Field Emission with Ultralow Turn On Voltage from Metal Decorated Carbon Nanotubes. *ACS Nano* **2014,** *8*, 7763-7770.

(147) Sridhar, S.; Ge, L.; Tiwary, C. S.; Hart, A. C.; Ozden, S.; Kalaga, K.; Lei, S.; Sridhar, S. V.; Sinha, R. K.; Harsh, H.; Kordas, K.; Ajayan, P. M.;

Vajtai, R. Enhanced Field Emission Properties from CNT Arrays Synthesized on Inconel Superalloy. *ACS Appl. Mater. Interfaces* **2014,** *6*, 1986-1991.

(148) Nguyen, D. D.; Tiwari, R. N.; Matsuoka, Y.; Hashimoto, G.; Rokuta, E.; Chen, Y.-Z.; Chueh, Y.-L.; Yoshimura, M. Low Vacuum Annealing of Cellulose Acetate on Nickel Towards Transparent Conductive CNT–Graphene Hybrid Films. *ACS Appl. Mater. Interfaces* **2014,** *6*, 9071-9077.

(149) Yuning, S.; Ki Nam, Y.; Guillaume, L.; Sang Heon, L.; Yoon-Ho, S.; Cheol Jin, L. High-performance field emission of carbon nanotube paste emitters fabricated using graphite nanopowder filler. *Nanotechnology* **2017,** *28*, 065201.

초 록

나노탄소 물질은 우수한 물성과 높은 종횡비의 구조적 장점을 갖고 있어 전계방출소재로 각광받고 있다. 다양한 제작방법을 통해 조립된 나노탄소 구조체는 나노스케일의 얇은 모서리와, 뾰족한 가시 구조 그리고 전기적, 열적, 화학적으로 강건한 물성을 통해 낮은 문턱전압, 고전류밀도, 장시간 동작안정성과 같은 우수한 성능을 나타낸다.

본 논문에서는 나노탄소 물질에 기반한 다차원 조립법을 통해 고성능 전계방출소자를 개발하였다. 1) 탄소나노튜브 기반 포인트 에미터를 제작하고 그래핀을 이용하여 금속-탄소나노튜브 계면 특성 극대화 연구를 수행하였다. 2) 탄소나노튜브 기반 라인형 에미터를 제작하여 대면적 고전류 방출 소자에 관한 연구를 수행하였다. 3) 그래핀 필름 기반 다공성 평판형 에미터를 제작하여 새로운 기작의 전계방출 소자 연구를 수행하였다. 4) 탄화코르크 기반의 다차원 에미터를 제작하여 낮은 문턱전압의 저전력 전계방출 소자 연구를 수행하였다. 본 연구를 통해 개발된 우수한 성능의 나노탄소 기반 전계방출소자는 X-ray, CT 단층촬영, 비파괴검사, 공항보안, 테라헤르츠 발진과 같은 다양한 응용이 가능할 뿐만 아니라, 소형·경량화를 통해 체내 삽입형 의료기기나 웨어러블 디바이스와 같은 미래형 응용이 기대된다.

주요어: 전계방출, 포인트 에미터, 라인형 에미터, 평판형 에미터, 계면, 그래핀, 탄소나노튜브, 문턱 전계, 전류 밀도

학 번: 2009-20709